

# HOMOGENIZATION OF PLASMONIC CRYSTALS: SEEKING THE EPSILON-NEAR-ZERO EFFECT

MATTHIAS MAIER\*, MARIOS MATTHEAKIS†, EFTHIMIOS KAXIRAS†‡,  
MITCHELL LUSKIN§, AND DIONISIOS MARGETIS¶

**Abstract.** By using an asymptotic analysis and numerical simulations, we derive and investigate a system of homogenized Maxwell’s equations for conducting material sheets that are periodically arranged and embedded in a heterogeneous and anisotropic dielectric host. This structure is motivated by the need to design plasmonic crystals that enable the propagation of electromagnetic waves with no phase delay (epsilon-near-zero effect). Our microscopic model incorporates the surface conductivity of the two-dimensional (2D) material of each sheet and a corresponding line charge density through a line conductivity along possible edges of the sheets. Our analysis generalizes averaging principles inherent in previous Bloch-wave approaches. We investigate physical implications of our findings. In particular, we emphasize the role of the vector-valued corrector field, which expresses microscopic modes of surface waves on the 2D material. We demonstrate how our homogenization procedure may set the foundation for computational investigations of: effective optical responses of reasonably general geometries, and complicated design problems in the plasmonics of 2D materials.

**1. Introduction.** The advent of two-dimensional (2D) materials with controllable electronic structures has opened up an unprecedented wealth of optical phenomena that challenge the classical diffraction limit of electromagnetic waves. Notable examples of related applications range from optical holography [40], tunable metamaterials [30], and cloaking [1], to subwavelength focusing lenses [9]. A striking feature of many of these applications is the possible emergence of an unusual parameter regime with no refraction, referred to as epsilon-near-zero (ENZ) effect [23, 25, 13, 27, 37].

This effect calls for designing novel *plasmonic crystals* made of stacked metallic or semi-metallic 2D material structures arranged periodically with subwavelength spacing, and embedded in a dielectric host [23, 25, 22, 8]. The growing need to describe, engineer, and tune the optical properties of such plasmonic crystals motivates the present paper. To gain insight into their effective optical behavior, we utilize a homogenization procedure that systematically illuminates how such macroscopic properties emerge from the plasmonic microstructure.

In this paper, our key objectives are: (i) to elucidate how effective parameter values of plasmonic crystals are derived from two-scale asymptotics; (ii) to demonstrate how this homogenization procedure can be used to compute effective optical responses of complicated (periodic) microstructures numerically; and (iii) to investigate physical implications of the resulting, effective description for a few prototypical geometries. The homogenized system can be controlled by tuning (microscopic) geometry, (periodic) spacing, frequency, and conductivity of the 2D material. This description implies precise conditions for the ENZ effect. Our work extends previous homogenization results for time-harmonic Maxwell’s equations [22, 39, 2, 3, 12]. In particular, we develop the following aspects of the homogenization of plasmonic crystals:

- We introduce a *general* homogenization result for a microscopic model that

---

\*Department of Mathematics, Texas A&M University, College Station, TX 77843, USA.

†John A. Paulson School of Engineering and Applied Sciences, Harvard University, Cambridge, MA 02138, USA.

‡Department of Physics, Harvard University, Cambridge, MA 02138, USA.

§School of Mathematics, University of Minnesota, Minneapolis, MN 55455, USA.

¶Department of Mathematics, and Institute for Physical Science and Technology, and Center for Scientific Computation and Mathematical Modeling, University of Maryland, College Park, MD 20910, USA.

incorporates the surface conductivity of arbitrarily curved 2D material sheets *and* a corresponding line charge density along possible edges of the sheets (see Section 2). The former may give rise to a *2D surface plasmon-polariton* (SPP) [24, 6] whereas the latter may influence the appearance of an *edge plasmon-polariton* (EPP) [15, 11]. These waves are special fine-scale surface and edge modes, respectively. The microscopic model describes a large class of plasmonic crystals consisting of periodic inclusions of metallic finite-size and curved 2D materials in a heterogeneous and anisotropic dielectric host (Sections 2, and 3).

- We demonstrate analytically how the combination of the complex-valued surface conductivity of the material sheets and the line conductivity along their edges can yield an ENZ effect (Section 4). In this framework, we derive precise ENZ conditions for planar sheets that extend results previously extracted from Bloch wave theory [25, 23]. In addition, by numerical simulations based on the finite element method, we discuss the ENZ effect occurring in a few prototypical geometries consisting of nanoscale 2D structures.
- We extend the homogenization procedure to include line charge models in correspondence to the line charge density of our microscopic description. This consideration accounts for possible edge effects. We discuss how this edge contribution extends known ENZ conditions (Section 4), and discuss further implications of this possibility in the conclusion (Section 6).
- We introduce a *computational platform* based on our homogenization procedure that can serve as a foundation for investigating the effective optical response of (reasonably general) microscopic geometries (Section 5). This framework enables the systematic computational investigation of complicated design problems in the plasmonics of 2D materials [28, 18, 26] (Sections 5 and 6).

We discuss several physical implications of our findings. For instance, we identify the physical role of the corrector field in our formulation: this field contains microscopic wave modes on the 2D material. We introduce a line charge density in the modeling and homogenization procedure, and show how the line charge density introduced in our microscopic model alters the ENZ effect of plasmonic crystals described previously [23, 25]. We recover a Lorentzian function for the effective dielectric permittivity tensor of selected prototypical geometries that partly validates our results since its real and imaginary parts automatically satisfy the Kramers-Kronig relations.

**1.1. Motivation: Epsilon-near-zero effect.** Recently, 2D materials such as graphene and black phosphorus have been the subject of extensive experimental and theoretical studies. From the viewpoint of Maxwell’s equations, the dielectric permittivity of a conducting 2D material may have a negative real part. As a result, SPPs of transverse-magnetic (TM) polarization may exist on the conducting sheet with a dispersion relation that allows for a transmitted wavenumber,  $k_{\text{SPP}}$ , much larger in magnitude than the free-space wavenumber,  $k_0$  [19].

Specifically, for an infinite, flat conducting sheet in an isotropic and homogeneous ambient space, the SPP dispersion relation is [24]

$$\sqrt{k_0^2 - k_{\text{SPP}}^2} = - \left( \frac{2k_0}{\omega\mu_0\sigma} \right) k_0,$$

where  $\sigma$  is the surface conductivity of the sheet,  $\mu_0$  is the magnetic permeability of the ambient space, and  $\omega$  denotes the angular frequency. Note that  $|k_{\text{SPP}}| \gg k_0$  if  $\text{Im } \sigma > 0$  and  $|\omega\mu_0\sigma| \ll k_0$  for an assumed  $e^{-i\omega t}$  time dependence and lossless

surrounding medium. Hence, the wavelength of the TM-polarized SPP scales linearly with  $\sigma$  if dissipation is relatively small ( $0 < \text{Re}\sigma \ll \text{Im}\sigma$ ).

In general, the dispersion relation of transmitted waves through given 2D materials can be altered dramatically by introducing different geometries of the sheet, or different arrangements of sheets in a dielectric host. In particular, plasmonic crystals are structures that consist of stacked, periodically aligned metallic layers. When the period is of the order of the SPP wavelength, unusual optical phenomena may occur, such as the ENZ effect and negative refraction [25, 21, 37, 27]. These properties can be precisely controlled by tuning the electronic structure of the 2D material, through chemical doping or other means, and the operating frequency,  $\omega$  [41, 36].

The ENZ effect implies that at least one eigenvalue of the *effective* dielectric permittivity of the plasmonic structure is close to zero. This effect causes surprising optical features, which have not been obtained by traditional photonic systems. These features include decoupling of spatial and temporal field variations, tunneling through very narrow channels, constant phase transmission, strong field confinement, diffraction-free propagation, and ultrafast phase transitions [37, 32]. Many novel functional devices based on plasmonic crystals have been proposed, indicating the broad prospects of photonics based on the ENZ effect [25, 21, 37, 27, 32, 41].

Motivated by this perspective, in this paper we develop a general homogenization procedure for plasmonic crystals. In addition, we investigate the possibility for emergence of the ENZ effect in prototypical geometries with, e.g., graphene layers, nanoribbons, and nanotubes.

**1.2. Microscopic model and geometry.** The geometry is shown in Figure 1. It consists of periodically stacked, possibly curved sheets,  $\Sigma^d$ , of a 2D material with surface conductivity  $\sigma^d(\mathbf{x})$ . We assume that a charge accumulation may occur via a *line conductivity*,  $\lambda^d(\mathbf{x})$ , on the edges  $\partial\Sigma^d$  of the sheets. The sheets are embedded in a dielectric with *heterogeneous* permittivity  $\varepsilon^d(\mathbf{x})$ . At the microscale, we invoke time-harmonic Maxwell's equations for the electromagnetic field  $(\mathbf{E}^d, \mathbf{H}^d)$  in domain  $\Omega$ ; see (2.1). The conductivities  $\sigma$  and  $\lambda$  are responsible for the induced current density

$$\mathbf{J}_{\Sigma^d} = \delta_{\Sigma^d} \sigma^d \mathbf{E}^d + \delta_{\partial\Sigma^d} \lambda^d \mathbf{E}^d.$$

Here,  $\delta_{\Sigma^d}$  denotes the Dirac delta function associated with the (possibly curved) surface of  $\Sigma^d$ , and  $\delta_{\partial\Sigma^d}$  is the Dirac delta function associated with the boundaries of  $\Sigma^d$ . The induced current density  $\mathbf{J}_{\Sigma^d}$  will lead to jump conditions of electromagnetic field components over  $\Sigma^d$  and  $\partial\Sigma^d$ . Detailed discussions and derivations of the governing equations and jump conditions are given in Section 2.

**1.3. Homogenized theory.** We will demonstrate by a formal *asymptotic analysis* that in the case of scale separation, meaning if  $d$  is sufficiently small compared to the free-space wavelength,  $2\pi/k_0$ , the above problem manifesting the microstructure can be expressed by the following *homogenized system*:

$$(1.1) \quad \nabla \times \mathcal{E} = i\omega\mu_0 \mathcal{H}, \quad \nabla \times \mathcal{H} = -i\omega\varepsilon^{\text{eff}} \mathcal{E} + \mathbf{J}_a,$$

in which the dependence on (microscale) spacing  $d$  is eliminated. Here,  $\mathbf{J}_a$  is a current-carrying source,  $(\mathcal{E}, \mathcal{H})$  describes an effective electromagnetic field, and  $\varepsilon^{\text{eff}}$  is an *effective permittivity tensor*.

We assume that the functions  $\varepsilon$ ,  $\sigma$  and  $\lambda$  depend on a slow scale and are periodic and rapidly oscillating on a (fast) scale proportional to the *scaling parameter*  $d$ ;

typically,  $d \ll 2\pi/k_0$ :

$$\varepsilon^d(\mathbf{x}) = \varepsilon(\mathbf{x}, \mathbf{x}/d), \quad \sigma^d = d \sigma(\mathbf{x}, \mathbf{x}/d), \quad \lambda^d = d^2 \lambda(\mathbf{x}, \mathbf{x}/d).$$

This scaling assumption leads to an effective permittivity tensor, viz.,

$$\begin{aligned} \varepsilon_{ij}^{\text{eff}} := & \int_Y \varepsilon(\mathbf{x}, \mathbf{y})(\mathbf{e}_j + \nabla_y \chi_j(\mathbf{x}, \mathbf{y})) \cdot \mathbf{e}_i \, d\mathbf{y} - \frac{1}{i\omega} \int_{\Sigma} \sigma(\mathbf{x}, \mathbf{y})(\mathbf{e}_j + \nabla_y \chi_j(\mathbf{x}, \mathbf{y})) \cdot \mathbf{e}_i \, d\mathbf{o}_y \\ & - \frac{1}{i\omega} \int_{\partial\Sigma} \lambda(\mathbf{x}, \mathbf{y})(\mathbf{e}_j + \nabla_y \chi_j(\mathbf{x}, \mathbf{y})) \cdot \mathbf{e}_i \, d\mathbf{s}. \end{aligned}$$

In the above equation,  $Y$  denotes the unit cell with embedded boundary  $\Sigma$  whose edge is  $\partial\Sigma$  (see Figure 1);  $\mathbf{e}_i$  is the unit vector in the  $i$ -th direction; and  $\nabla_y \chi$  is the Jacobian of the *corrector*,  $\chi$ , that solves the associated cell problem which encodes the microscopic details, cf. (3.2). A crucial property of  $\varepsilon^{\text{eff}}$  is that it manifests an interplay, and possible mutual cancellation, of three distinct averages. Thus, by tuning geometry, (periodic) spacing, frequency and conductivities of the 2D material, we can force one or more eigenvalues of  $\varepsilon^{\text{eff}}$  to be close to zero. This ENZ effect is detailed in Section 4.

**1.4. Past works.** The derivation presented in this paper is based on a formal asymptotic analysis in the spirit of [5]. Note that in [22] a rigorous approach invoking two-scale convergence is applied to plasmonic crystals without a line charge density along edges. In the framework of homogenization theory for time-harmonic Maxwell's equations, we should also mention a number of other related, rigorous or formal, results [31, 39, 12, 2, 3]. In particular, in [12] a formal asymptotic analysis is applied to *finite* photonic crystals; and in [31] the authors homogenize Maxwell's equations in the presence of rough boundaries (see also [16]).

Broadly speaking, the design of structures with unusual optical properties is a highly active direction of research. For recent advances in photonics, we refer the reader to [14, 42]. In fact, the computation of effective material parameters in Maxwell's equations has a long history in physics and engineering. It is impossible to exhaustively list the related bibliography here. In regard to the homogenization of periodic and heterogeneous systems, we mention as examples [16, 35, 8, 17].

Notably, homogenization results for Maxwell's equations can be related to approaches based on *Bloch theory* for waves in periodic structures. In Section 4, we demonstrate that our homogenization result readily generalizes an averaging principle that was previously found in particular Bloch-wave solutions constructed for simple settings [23, 25]. In the context of layered structures usually only a few Bloch waves effectively contribute to the macroscopic field [38]. In contrast, our approach relies entirely on periodic upscaling principles and is thus *independent* of the choice of particular solutions. In fact, we derive effective equations and material parameters that are valid for a wide range of geometries without choosing any particular solutions *a priori*.

**1.5. Limitations.** Although the homogenization results presented in this paper are fairly general, our analysis bears limitations. We should mention the following issues:

- Our analysis leaves out *boundary effects* in the homogenization procedure due to the interaction of the microstructure (conducting sheet) with boundaries of the domain. This simplification restricts the homogenization result either to layered microstructures immersed in a scattering domain, or to domains with periodic boundary conditions.

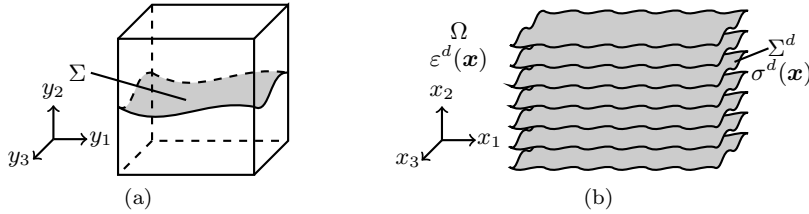


Fig. 1: Schematic of geometry. (a) The unit cell,  $Y = [0, 1]^3$ , with microstructure  $\Sigma$ , a conducting sheet. (b) Computational domain  $\Omega$  with rescaled periodic layers  $\Sigma^d$  and spatially dependent surface conductivity  $\sigma^d(\mathbf{x})$ . The ambient medium has a heterogeneous permittivity,  $\varepsilon^d(\mathbf{x})$ .

- Our asymptotic analysis relies on a strong periodicity assumption for the microstructure. Even though we allow material parameters to also depend on a slow scale, we do not account for a slowly varying geometry of the microstructure.
- We assume a scale separation between the free-space wavenumber,  $k_0$ , which we treat as of the order of unity ( $k_0 \sim 1$ ), and the *SPP wavenumber*,  $k_{\text{SPP}}$ , with  $k_{\text{SPP}} \sim 1/d$ . This assumption rules out resonance effects, if the period (spacing),  $d$ , is close to the free-space wavelength. In this vein, we do not discuss the case with resonant scaling,  $k_{\text{SPP}} \sim 1$ .

**1.6. Paper organization.** The remainder of the paper is organized as follows. In Section 2, we introduce the microscale model and scaling assumptions. In Section 3, we derive a system of homogenized equations and the corresponding cell problem, which determine the effective material parameters. Section 4 provides a detailed discussion of the ENZ effect from our homogenization. In Section 5, we complement our analytical findings by a demonstration via examples of how the homogenization results can serve as a platform for computing the effective optical response of various microscopic geometries. Section 6 concludes the paper with a summary of the key results and an outline of open problems. In the appendix we provide detailed analytical derivations needed in the main text, for the sake of brevity. The supplementary material contains some additional analytical derivations that are not essential for our paper. We use the  $e^{-i\omega t}$  time dependence throughout.

**2. Microscopic theory and geometry.** In this section, we give a detailed description of the (full) microscale model and geometry. We also describe our scaling assumptions and discuss the rationale underlying them.

Our objective is to study Maxwell’s equations in the (not necessarily bounded) domain  $\Omega \subset \mathbb{R}^3$  that contains microstructures with periodically aligned, plasmonic hypersurfaces  $\Sigma^d$ ; see Figure 1. These hypersurfaces are generated from the inscribed hypersurface  $\Sigma$  via scaling with a length scale,  $d$ , and periodically repeating a *unit cell*,  $Y = [0, 1]^3$ . More precisely, we define

$$\Sigma^d = \{d\mathbf{z} + d\boldsymbol{\varsigma} : \mathbf{z} \in \mathbb{Z}^3, \boldsymbol{\varsigma} \in \Sigma\},$$

where  $\mathbb{Z}$  denotes the set of integers. Note that we make no specific assumption about  $\Sigma$ , except that it is smooth (in  $Y$  and when periodically continued) so that it admits a well-defined surface normal. This property does neither imply that  $\Sigma$  has to be a

connected manifold, nor that  $\Sigma$  has to have an intersection with the boundary of  $Y$ ; see Section 5 for examples.

The relevant material parameters can be heterogeneous and tensor-valued. We assume that the ambient medium, which is contained in  $\Omega \setminus \Sigma^d$ , is described by a dielectric permittivity,  $\varepsilon^d(\mathbf{x})$ . Furthermore, the plasmonic sheets  $\Sigma^d$  have the associated surface conductivity  $\sigma^d(\mathbf{x})$ . In addition, we allow for a *line conductivity*  $\lambda^d(\mathbf{x})$  on the edges,  $\partial\Sigma^d$ , of the sheets.

To derive a physically appealing homogenization limit, we assume that the spatial dependence of the material parameters can be separated into a slowly oscillating macroscale behavior and a (locally) periodic microscale behavior with structural period  $d$  [5, 34], viz.,

$$\varepsilon^d(\mathbf{x}) = \varepsilon(\mathbf{x}, \mathbf{x}/d), \quad \sigma^d(\mathbf{x}) = d\sigma(\mathbf{x}, \mathbf{x}/d), \quad \lambda^d(\mathbf{x}) = d^2\lambda(\mathbf{x}, \mathbf{x}/d).$$

Here,  $\varepsilon(\mathbf{x}, \cdot)$ ,  $\sigma(\mathbf{x}, \cdot)$ , and  $\lambda(\mathbf{x}, \cdot)$  are  $Y$ -periodic and tensor-valued, i.e.,  $\varepsilon(\mathbf{x}, \mathbf{y} + \mathbf{e}_i) = \varepsilon(\mathbf{x}, \mathbf{y})$ ,  $\sigma(\mathbf{x}, \mathbf{y} + \mathbf{e}_i) = \sigma(\mathbf{x}, \mathbf{y})$ , and  $\lambda(\mathbf{x}, \mathbf{y} + \mathbf{e}_i) = \lambda(\mathbf{x}, \mathbf{y})$ , for any unit vector  $\mathbf{e}_i$  and  $\mathbf{x} \in \Omega$ ,  $\mathbf{y} \in \mathbb{R}^3$ .

The surface conductivity  $\sigma(\mathbf{x}, \mathbf{y})$  and line conductivity  $\lambda(\mathbf{x}, \mathbf{y})$  deserve particular attention. The former describes the linear optical response of the (possibly curved) hypersurface  $\Sigma$ , or induced surface current along  $\Sigma$ , due to an incident electric field. Similarly,  $\lambda$  describes the linear response of the edges,  $\partial\Sigma$ , of  $\Sigma$ , or induced line current along  $\partial\Sigma$ , due to an incident electric field. These considerations imply that both tensors,  $\sigma(\mathbf{x}, \mathbf{y})$  and  $\lambda(\mathbf{x}, \mathbf{y})$ , are rank deficient with one, or two zero eigenvalues, respectively. More precisely, by fixing  $(\mathbf{x}, \mathbf{y})$  and expressing the tensors  $\sigma(\mathbf{x}, \mathbf{y})$  and  $\lambda(\mathbf{x}, \mathbf{y})$  in local coordinates  $(\boldsymbol{\tau}, \mathbf{n}, \boldsymbol{\nu})$ , where  $\boldsymbol{\tau}$  is a vector field parallel to the edge  $\partial\Sigma$ ,  $\boldsymbol{\nu}$  is the (interior) normal on  $\Sigma^d$ , and  $\mathbf{n}$  denotes the outward-pointing unit vector orthogonal to  $\boldsymbol{\tau}$  and  $\boldsymbol{\nu}$ , we have

$$\sigma^d = \begin{pmatrix} \sigma_{11} & \sigma_{12} & 0 \\ \sigma_{21} & \sigma_{22} & 0 \\ 0 & 0 & 0 \end{pmatrix}, \quad \lambda^d = \begin{pmatrix} \lambda_{11} & 0 & 0 \\ 0 & 0 & 0 \\ 0 & 0 & 0 \end{pmatrix}.$$

Since we will apply a formal asymptotic analysis, our assumptions on the related parameters are not too restrictive. Consequently, we use arbitrary tensor-valued functions  $\varepsilon$  and  $\sigma$ . A mathematically rigorous convergence result typically requires more restrictive assumptions [22].

**2.1. On the scaling of conductivities.** Our particular choice of scalings of the surface and line conductivities with  $d$ , viz.,

$$\sigma^d \sim d, \quad \lambda^d \sim d^2,$$

deserves some explanation. We recall that the wavenumber,  $k_{\text{SPP}}$ , of the desired, fine-scale SPP on an infinite conducting sheet scales inversely proportional to the surface conductivity (Section 1). Hence, our choice of scaling of  $\sigma^d$  distinctly separates two scales: one related to the free-space wavenumber  $k_0$  ( $k_0 \sim 1$ ), determined by the average of  $\varepsilon^d$ , and another for the SPP wavenumber,  $k_{\text{SPP}} \sim 1/\sigma^d \sim 1/d$ , on the conducting sheets [21]. By our scaling, the *interaction range* of the SPP on each sheet is of the order of  $d$ . More precisely, in the limit  $d \rightarrow 0$  the strength with which SPPs on one sheet influence neighboring sheets remains constant. In addition, our choice of scaling implies that the total surface current on the sheets remains *finite*. In a similar vein we scale the line conductivity,  $\lambda^d$ , with  $d^2$ . In the limit  $d \rightarrow 0$ , this assumption yields a *finite* total line current on the edges of the conducting sheets.

It is worth mentioning that other scaling scenarios may lead to different homogenization results. For example, the assumption  $\sigma^d \sim 1$  corresponds to a resonance which in turn yields an effective *permeability* tensor [7]. Such a configuration can exhibit a respective *mu-near-zero* effect. A variety of structures, e.g., nanorings, that exhibit a mu-near-zero effect are studied in [33].

**2.2. Heterogeneous Maxwell's equations.** The time-harmonic Maxwell equations for the electromagnetic field  $(\mathbf{E}^d, \mathbf{H}^d)$  in  $\Omega \setminus \Sigma^d$  are:

$$(2.1) \quad \begin{cases} \nabla \times \mathbf{E}^d = i\omega\mu_0\mathbf{H}^d, & \nabla \times \mathbf{H}^d = -i\omega\varepsilon^d\mathbf{E}^d + \mathbf{J}_a, \\ \nabla \cdot (\varepsilon^d\mathbf{E}^d) = \frac{1}{i\omega}\nabla \cdot \mathbf{J}_a, & \nabla \cdot \mathbf{H}^d = 0. \end{cases}$$

The surface conductivity,  $\sigma^d$ , is responsible for the appearance of the current density  $\mathbf{J}_{\Sigma^d} = \delta_{\Sigma^d}\sigma^d\mathbf{E}^d$ , on  $\Sigma^d$ . Accordingly, we must impose the following jump conditions on  $\Sigma^d$  (away from the boundaries  $\partial\Sigma^d$ ):

$$(2.2) \quad \begin{cases} [\boldsymbol{\nu} \times \mathbf{E}^d]_{\Sigma^d} = 0, & [\boldsymbol{\nu} \times \mathbf{H}^d]_{\Sigma^d} = \sigma^d\mathbf{E}^d, \\ [\boldsymbol{\nu} \cdot (\varepsilon^d\mathbf{E}^d)]_{\Sigma^d} = \frac{1}{i\omega}\nabla \cdot (\sigma^d\mathbf{E}^d), & [\boldsymbol{\nu} \cdot \mathbf{H}^d]_{\Sigma^d} = 0. \end{cases}$$

Here,  $[\cdot]_{\Sigma^d}$  denotes the jump over  $\Sigma^d$  with respect to a chosen normal  $\boldsymbol{\nu}$ , viz.,

$$[\mathbf{F}]_{\Sigma^d}(\mathbf{x}) := \lim_{\alpha \searrow 0} (\mathbf{F}(\mathbf{x} + \alpha\boldsymbol{\nu}) - \mathbf{F}(\mathbf{x} - \alpha\boldsymbol{\nu})) \quad \mathbf{x} \in \Sigma^d.$$

Equations (2.1) and (2.2) are supplemented with the following internal boundary conditions on the edges of the plasmonic sheets,  $\Sigma^d$ , due to the line conductivity  $\lambda^d$ :

$$(2.3) \quad \begin{cases} \left\{ \mathbf{n} \times \mathbf{H}^d \right\}_{\partial\Sigma^d} = \lambda^d\mathbf{E}^d, \\ \mathbf{n} \cdot (\sigma^d\mathbf{E}^d) = \nabla \cdot (\lambda^d\mathbf{E}^d) \quad \text{on } \partial\Sigma^d, \end{cases}$$

where  $\mathbf{n}$  denotes the outward-pointing unit vector tangential to the 2D sheet  $\Sigma^d$  and normal to curve  $\partial\Sigma^d$ . In (2.3), the symbol  $\{\cdot\}_{\partial\Sigma^d}$  denotes a *singular* jump over the edge,  $\partial\Sigma^d$ , viz.,

$$(2.4) \quad \left\{ \mathbf{F} \right\}_{\partial\Sigma^d}(\mathbf{x}) := \lim_{\alpha \searrow 0} \int_{-\alpha}^{\alpha} (\mathbf{F}(\mathbf{x} + \alpha^2\mathbf{n} + \zeta\boldsymbol{\nu}) - \mathbf{F}(\mathbf{x} - \alpha^2\mathbf{n} + \zeta\boldsymbol{\nu})) d\zeta \quad \mathbf{x} \in \partial\Sigma^d.$$

The jump condition in (2.3) stems from the property that, by virtue of the Ampère-Maxwell law, the line current  $\lambda^d\mathbf{E}^d$  creates a *singular* magnetic field,  $\mathbf{H} \sim (1/r)\mathbf{e}_\varphi$  as  $r \rightarrow 0$ , where  $r$  denotes the distance to the edge,  $\partial\Sigma^d$ , and  $\mathbf{e}_\varphi$  is the unit vector in the azimuthal direction of the local cylindrical coordinate system. In this sense, jump (2.4) measures the strength of the singularity of the magnetic field  $\mathbf{H}$  at any point  $\mathbf{x} \in \partial\Sigma^d$ . We refer the reader to Section B of the supplementary material for a detailed discussion including a derivation of the jump  $\{\cdot\}_{\partial\Sigma^d}$ .

The second compatibility condition in (2.3) is a direct consequence of charge conservation along the edges,  $\partial\Sigma^d$ , in view of the fact that  $\sigma^d$  vanishes identically outside the sheets. Let us explain. The *line charge accumulation* at the edges is related to the jump of the electric displacement field in the  $\mathbf{n}$ -direction over the edge,



$\partial\Sigma^d$ . This jump is in turn equal to  $(i\omega)^{-1}\mathbf{n} \cdot (\sigma^d \mathbf{E}^d)$ , since  $\sigma^d \equiv 0$  outside  $\Sigma^d$ . The corresponding line conductivity must be balanced by the divergence of the line current  $\lambda^d \mathbf{E}^d$ . Alternatively, compatibility conditions (2.3) can be derived from a variational formulation; see Section C of the supplementary material.

Equations (2.1)–(2.3) form a closed system if they are complemented by suitable boundary conditions on  $\partial\Omega$ . We can impose either *absorbing* conditions, or *periodic* conditions, or, in the case with an unbounded domain,  $\Omega$ , Silver-Müller radiation conditions at infinity [29, 24]. We make the important assumption that the domain,  $\Omega$ , and the chosen boundary conditions on  $\partial\Omega$  are compatible with the microstructure in the sense of the following simultaneous requirements: (i) the microstructure is bounded, that is  $\sigma(\mathbf{x}, \cdot) = 0$  and  $\varepsilon(\mathbf{x}, \cdot) = \varepsilon_0$  for  $|\mathbf{x}| \geq C$  for some  $C > 0$ ; and (ii) the microstructure only touches those parts of the boundary  $\partial\Omega$  with periodic boundary conditions. These requirements ensure that the formal homogenization result derived in this paper remains valid everywhere. If any one of these requirements is not satisfied, a *boundary layer* might occur, which necessitates a subtle homogenization procedure near  $\partial\Omega$  [34].

**3. Two-scale expansions and asymptotics.** In this section, we provide a derivation of effective system (1.1) by means of a formal asymptotic analysis. For the sake of brevity, we summarize the derivation here and refer the reader to Appendix A for details.

We start with the microscale description of (2.1), (2.2) and (2.3). Consider the two-scale expansions [5, 34]

$$\begin{aligned} \mathbf{E}^d &\rightarrow \mathbf{E}^{(0)}(\mathbf{x}, \mathbf{y}) + d\mathbf{E}^{(1)}(\mathbf{x}, \mathbf{y}) + d^2\mathbf{E}^{(2)}(\mathbf{x}, \mathbf{y}) + \dots, \\ \mathbf{H}^d &\rightarrow \mathbf{H}^{(0)}(\mathbf{x}, \mathbf{y}) + d\mathbf{H}^{(1)}(\mathbf{x}, \mathbf{y}) + d^2\mathbf{H}^{(2)}(\mathbf{x}, \mathbf{y}) + \dots, \end{aligned}$$

with the corresponding substitutions

$$\nabla \rightarrow \nabla_{\mathbf{x}} + \frac{1}{d}\nabla_{\mathbf{y}}, \quad \varepsilon^d \rightarrow \varepsilon(\mathbf{x}, \mathbf{y}), \quad \sigma^d \rightarrow d\sigma(\mathbf{x}, \mathbf{y}), \quad \lambda^d \rightarrow d^2\lambda(\mathbf{x}, \mathbf{y}).$$

Here,  $\mathbf{y} \in Y$  denotes the fast variable, a now *independent* coordinate for the microscale. The small parameter,  $d$ , is treated as non-dimensional since it is scaled with  $1/k_0$  which is set to unity.

The application of the above formal expansions to (2.1) and (2.2) and the subsequent dominant balance need to be carried out to the two lowest orders in the small parameter,  $d$ . This procedure results in eight equations and eight boundary conditions ((A.1)–(A.3) in Appendix A), as well as two interface conditions on  $\partial\Sigma$  ((A.4)–(A.5) in Appendix A). We now use the expanded equations to describe  $\mathbf{E}^{(0)}$  and  $\mathbf{H}^{(0)}$  (see (A.6)–(A.7) in Appendix A; cf. [22]). Thus, we find

$$(3.1) \quad \begin{cases} \mathbf{E}^{(0)}(\mathbf{x}, \mathbf{y}) = \mathcal{E}(\mathbf{x}) + \nabla_{\mathbf{y}}\varphi(\mathbf{x}, \mathbf{y}), & \varphi(\mathbf{x}, \mathbf{y}) = \sum_{j=1}^3 \chi_j(\mathbf{x}, \mathbf{y})\mathcal{E}_j(\mathbf{x}), \\ \mathbf{H}^{(0)}(\mathbf{x}, \mathbf{y}) = \mathcal{H}(\mathbf{x}), \end{cases}$$

where  $\chi_j(\mathbf{x}, \cdot)$  are the correctors and assumed to be  $Y$ -periodic ( $j = 1, 2, 3$ ).

Next, we focus on the functions  $\mathcal{E}(\mathbf{x})$ ,  $\mathcal{H}(\mathbf{x})$  and  $\chi_j(\mathbf{x}, \mathbf{y})$  ( $j = 1, 2, 3$ ). For this purpose, we resort to the corresponding *cell problem* (see Section AA.2 in Appendix A).



Each  $\chi_j(\mathbf{x}, \mathbf{y})$  satisfies

$$(3.2) \quad \begin{cases} \nabla_{\mathbf{y}} \cdot \left( \varepsilon(\mathbf{x}, \mathbf{y})(\mathbf{e}_j + \nabla_{\mathbf{y}} \chi_j(\mathbf{x}, \mathbf{y})) \right) = 0 & \text{in } Y \setminus \Sigma, \\ [\boldsymbol{\nu} \times (\mathbf{e}_j + \nabla_{\mathbf{y}} \chi_j(\mathbf{x}, \mathbf{y}))]_{\Sigma} = 0 & \text{on } \Sigma, \\ \left[ \boldsymbol{\nu} \cdot \left( \varepsilon(\mathbf{x}, \mathbf{y})(\mathbf{e}_j + \nabla_{\mathbf{y}} \chi_j(\mathbf{x}, \mathbf{y})) \right) \right]_{\Sigma} = \frac{1}{i\omega} \nabla_{\mathbf{y}} \cdot \left( \sigma(\mathbf{x}, \mathbf{y})(\mathbf{e}_j + \nabla_{\mathbf{y}} \chi_j(\mathbf{x}, \mathbf{y})) \right) & \text{on } \Sigma, \\ \mathbf{n} \cdot \left( \sigma(\mathbf{x}, \mathbf{y})(\mathbf{e}_j + \nabla_{\mathbf{y}} \chi_j(\mathbf{x}, \mathbf{y})) \right) = \nabla_{\mathbf{y}} \cdot \left( \lambda(\mathbf{x}, \mathbf{y})(\mathbf{e}_j + \nabla_{\mathbf{y}} \chi_j(\mathbf{x}, \mathbf{y})) \right) & \text{on } \partial\Sigma \setminus \partial Y. \end{cases}$$

Equations (3.2) along with the condition that  $\chi_j(\mathbf{x}, \cdot)$  be  $Y$ -periodic form the desired, closed cell problem. Notice that  $\mathbf{x}$  plays the role of a parameter. Hence, the above cell problem uniquely describes  $\chi_j(\mathbf{x}, \cdot)$  for any given (macroscopic) point  $\mathbf{x}$ .

A remark on the two jump conditions in (3.2) is in order. The first jump condition ensures that the tangential part of  $\mathbf{e}_j + \nabla_{\mathbf{y}} \chi_j(\mathbf{x}, \mathbf{y})$  on  $\Sigma$  is single valued. In regard to the second jump condition, recall that  $\sigma(\mathbf{x}, \mathbf{y})$  only acts on the tangential part of a vector field (to return a tangential vector). Thus, the right-hand side of the respective jump condition consists of the divergence of tangential field components, which in turn implies that this term is also single valued.

Similarly, we recover the *homogenized system* that fully describes  $\boldsymbol{\mathcal{E}}$  and  $\boldsymbol{\mathcal{H}}$ , viz.,

$$(3.3) \quad \begin{cases} \nabla \times \boldsymbol{\mathcal{E}} = i\omega\mu_0 \boldsymbol{\mathcal{H}}, & \nabla \times \boldsymbol{\mathcal{H}} = -i\omega \varepsilon^{\text{eff}} \boldsymbol{\mathcal{E}} + \mathbf{J}_a; \\ \nabla \cdot (\varepsilon^{\text{eff}} \boldsymbol{\mathcal{E}}) = \frac{1}{i\omega} \nabla \cdot \mathbf{J}_a, & \nabla \cdot \boldsymbol{\mathcal{H}} = 0, \end{cases}$$

with the *effective permittivity tensor*  $\varepsilon^{\text{eff}}$  given by

$$(3.4) \quad \varepsilon_{ij}^{\text{eff}}(\mathbf{x}) := \int_Y \varepsilon(\mathbf{x}, \mathbf{y})(\mathbf{e}_j + \nabla_{\mathbf{y}} \chi_j(\mathbf{x}, \mathbf{y})) \cdot \mathbf{e}_i \, d\mathbf{y} - \frac{1}{i\omega} \int_{\Sigma} \sigma(\mathbf{x}, \mathbf{y})(\mathbf{e}_j + \nabla_{\mathbf{y}} \chi_j(\mathbf{x}, \mathbf{y})) \cdot \mathbf{e}_i \, d\mathbf{o}_{\mathbf{y}} - \frac{1}{i\omega} \int_{\partial\Sigma \setminus \partial Y} \lambda(\mathbf{x}, \mathbf{y})(\mathbf{e}_j + \nabla_{\mathbf{y}} \chi_j(\mathbf{x}, \mathbf{y})) \cdot \mathbf{e}_i \, d\mathbf{s}.$$

For the sake of brevity, we give the derivation of this formula to Section AA.3 of Appendix A.

Equations (3.1)–(3.4) summarize our main homogenization results. In conclusion, system (3.3) describes the large-scale optical response of the periodic medium in terms of the macroscopic electromagnetic field  $(\boldsymbol{\mathcal{E}}, \boldsymbol{\mathcal{H}})$  via the effective permittivity tensor  $\varepsilon^{\text{eff}}$  given by (3.4) with (3.2).

**4. Epsilon-near-zero effect.** A crucial feature of the averaging for the effective permittivity,  $\varepsilon^{\text{eff}}(\mathbf{x})$ , as implied by (3.4), is the *interplay* of three distinct averages: one for the bulk permittivity,  $\varepsilon$ ; another for the surface conductivity,  $\sigma$ ; and a third one for the line conductivity,  $\lambda$ . Each of these averages has a positive real part. This interplay can be exploited as follows. By tuning the microscopic geometry, periodic spacing, frequency, or surface or line conductivity, we can in principle force at least one eigenvalue of  $\varepsilon^{\text{eff}}(\mathbf{x})$  to be close to zero. In the case with an  $\mathbf{x}$ -independent  $\varepsilon^{\text{eff}}$ , this condition amounts to the ENZ effect in the direction of propagation determined by the respective eigenvector(s) [23, 25].

In the remainder of this section, we discuss the simplified case with a vanishing corrector,  $\chi$ . In this case, we derive an explicit formula for the special spacing,  $d = d_c$ , called the critical spacing, that implies the ENZ effect in the presence of the line conductivity,  $\lambda$ . We show how our present averaging procedure is related to results of a Bloch-wave approach [23]. Lastly, we discuss in some detail the character and physical role of the corrector,  $\chi$ .

**4.1. Case with vanishing corrector  $\chi$ : Formalism.** In principle, the corrector,  $\chi$ , implicitly depends on the geometry and material parameters such as  $\sigma$  and  $\lambda$ . Accordingly, the derivation of closed, analytical formulas for  $\chi$  may be possible only in a limited number of situations. We now restrict attention to the particular yet physically appealing case with a vanishing corrector,  $\chi$ . Our goal is to better understand the emerging ENZ effect.

Technically speaking, the solution,  $\chi$ , of cell problem (3.2) vanishes whenever the forcing term in this problem is identically zero. This term may not be immediately obvious by inspection of (3.2). In order to gain some insight into its character, we invoke the weak formulation of the cell problem. To this end, we multiply the first equation in (3.2) with a smooth and  $Y$ -periodic test function,  $\psi$ , and integrate over  $Y$  (see also Section C of the supplementary material). Two subsequent integrations by parts, and use of the requisite jump and boundary conditions, yield

$$\begin{aligned} 0 = & \int_Y \varepsilon(\mathbf{x}, \mathbf{y}) (\mathbf{e}_j + \nabla_y \chi_j(\mathbf{x}, \mathbf{y})) \cdot \nabla_y \psi(\mathbf{y}) \, d\mathbf{y} \\ & - \frac{1}{i\omega} \int_{\Sigma} \sigma(\mathbf{x}, \mathbf{y}) (\mathbf{e}_j + \nabla_y \chi_j(\mathbf{x}, \mathbf{y})) \cdot \nabla_y \psi(\mathbf{y}) \, d\mathbf{o}_y \\ & - \frac{1}{i\omega} \int_{\partial\Sigma \setminus \partial Y} \lambda(\mathbf{x}, \mathbf{y}) (\mathbf{e}_j + \nabla_y \chi_j(\mathbf{x}, \mathbf{y})) \cdot \nabla_y \psi(\mathbf{y}) \, ds . \end{aligned}$$

The forcing term corresponds to the following contribution:

$$(4.1) \quad \int_Y \varepsilon(\mathbf{x}, \mathbf{y}) \mathbf{e}_j \cdot \nabla_y \psi(\mathbf{y}) \, d\mathbf{y} - \frac{1}{i\omega} \int_{\Sigma} \sigma(\mathbf{x}, \mathbf{y}) \mathbf{e}_j \cdot \nabla_y \psi(\mathbf{y}) \, d\mathbf{o}_y - \frac{1}{i\omega} \int_{\partial\Sigma \setminus \partial Y} \lambda(\mathbf{x}, \mathbf{y}) \mathbf{e}_j \cdot \nabla_y \psi(\mathbf{y}) \, ds . \quad \blacksquare$$

Thus, the requirement of having a vanishing corrector means that (4.1) must vanish identically for every possible choice of  $\psi$ . One more integration by parts converts expression (4.1) to

$$\begin{aligned} i\omega \int_Y \nabla_y \cdot (\varepsilon(\mathbf{x}, \mathbf{y}) \mathbf{e}_j) \psi(\mathbf{y}) \, d\mathbf{y} + \int_{\partial\Sigma} \mathbf{n} \cdot (\sigma(\mathbf{x}, \mathbf{y}) \mathbf{e}_j) \psi(\mathbf{y}) \, ds \\ - \int_{\Sigma} \nabla_y \cdot (\sigma(\mathbf{x}, \mathbf{y}) \mathbf{e}_j) \psi(\mathbf{y}) \, d\mathbf{o}_y - \int_{\partial\Sigma \setminus \partial Y} \nabla_y \cdot (\lambda(\mathbf{x}, \mathbf{y}) \mathbf{e}_j) \psi(\mathbf{y}) \, ds . \end{aligned}$$

Thus, the forcing is necessarily zero whenever the following conditions hold simultaneously:

$$(4.2) \quad \begin{cases} \nabla_y \cdot \varepsilon(\mathbf{x}, \mathbf{y}) = 0 & \text{in } Y , \\ \nabla_y \cdot \sigma(\mathbf{x}, \mathbf{y}) = 0 & \text{on } \Sigma , \\ \mathbf{n} \cdot \sigma(\mathbf{x}, \mathbf{y}) - \nabla_y \cdot \lambda(\mathbf{x}, \mathbf{y}) = 0 & \text{on } \partial\Sigma \setminus \partial Y . \end{cases}$$

Note that  $\sigma$  and  $\lambda$  encode information about the curvature of  $\Sigma$  and  $\partial\Sigma$ , respectively. This implies that for a non-flat surface  $\Sigma$ , or for a surface with (arbitrarily shaped) internal edges,  $\sigma(\mathbf{x}, \mathbf{y})$  and  $\lambda(\mathbf{x}, \mathbf{y})$  are in principle  $\mathbf{y}$ -dependent with non-vanishing divergence. Under the assumption that (4.2) holds, formula (3.4) for the effective permittivity simply reduces to

$$(4.3) \quad \varepsilon^{\text{eff}} = \int_Y \varepsilon(\mathbf{x}, \mathbf{y}) \, d\mathbf{y} - \frac{1}{i\omega} \int_{\Sigma} \sigma(\mathbf{x}, \mathbf{y}) \, do_{\mathbf{y}} - \frac{1}{i\omega} \int_{\partial\Sigma \setminus \partial Y} \lambda(\mathbf{x}, \mathbf{y}) \, ds .$$

By this simplified (geometric) average, one may directly influence the effective permittivity tensor by either adjusting the operating frequency,  $\omega$ , or by tuning the parameters  $\sigma(\mathbf{x}, \mathbf{y})$  and  $\lambda(\mathbf{x}, \mathbf{y})$ .

We add a remark on the above formalism. A natural question at this point concerns the existence of suitable configurations that obey (4.2). More precisely, it is of interest to specify configurations that allow for a vanishing corrector while two or all three of the distinct averages in (4.3) are nonzero. We give three related examples in this section. First, consider the geometry with parallel, planar sheets of constant  $\sigma$  and no edges,  $\partial\Sigma = \emptyset$ , embedded in a homogeneous dielectric host with uniform  $\varepsilon$ ; see Figure 2a. In this case,  $\chi \equiv 0$ , and we can have a nonzero contribution from the average of  $\sigma$  in (4.3). The second geometry consists of parallel and periodically aligned nanoribbons embedded in a homogeneous, dielectric host; see Figure 2b. In this case, we can achieve  $\chi \equiv 0$  through (4.2) and a nonzero contribution of the line average of  $\lambda$  in (4.3) by setting  $\sigma^d = 0$  and choosing a constant  $\lambda^d$ . Further, in the same geometry, by choosing a constant  $\sigma$  and the  $y_3$ -dependent line conductivity  $\lambda = \sigma y_3$ , all three averages in (4.3) are nonzero while condition (4.2) holds; thus,  $\chi \equiv 0$ . An example with a geometry that always has a nonzero corrector (in the presence of a nonzero conductivity  $\sigma$ ) consists of parallel and periodically aligned nanotubes; see Figure 2c. For this third case, the corrector  $\chi$  is obtained numerically. (For further discussion on the computational framework for  $\chi$ , the interested reader is referred to Section 5.)

**4.2. Vanishing corrector: A notion of critical spacing.** In this subsection, we further simplify average (4.3) in order to derive an explicit formula for the critical spacing,  $d_c$ . Recall the ansatz

$$\sigma^d(\mathbf{x}) = d\sigma(\mathbf{x}, \mathbf{x}/d), \quad \lambda^d(\mathbf{x}) = d^2\lambda(\mathbf{x}, \mathbf{x}/d) ;$$

see Section 1.2.1. Although this choice of scaling is convenient for the asymptotic analysis (Section 3), it introduces two parameters,  $\sigma$  and  $\lambda$ , that couple the physical conductivities,  $\sigma^d$  and  $\lambda^d$ , with the spacing,  $d$ . This coupling may obscure the physical insight possibly gained by the averaging in (4.3). A reason is that, in realistic settings, the parameters  $d$ ,  $\sigma^d$  and  $\lambda^d$  are controlled independently by tuning of the geometry and the electronic structure of the 2D material [25].

As a remedy, consider the following rescaled quantities

$$\sigma^d(\mathbf{x}, \mathbf{y}) := d\sigma(\mathbf{x}, \mathbf{y}) , \quad \lambda^d(\mathbf{x}, \mathbf{y}) := d^2\lambda(\mathbf{x}, \mathbf{y}) ,$$

where the microscale variable,  $y$ , is singled out and treated as independent in the actual conductivities,  $\sigma^d(\mathbf{x})$  and  $\lambda^d(\mathbf{x})$ . The averages of interest therefore are

$$\bar{\varepsilon}(\mathbf{x}) = \int_Y \varepsilon(\mathbf{x}, \mathbf{y}) \, d\mathbf{y} , \quad \bar{\sigma}^d(\mathbf{x}) = \int_{\Sigma} \sigma^d(\mathbf{x}, \mathbf{y}) \, do_{\mathbf{y}} , \quad \bar{\lambda}^d(\mathbf{x}) = \int_{\partial\Sigma \setminus \partial Y} \lambda^d(\mathbf{x}, \mathbf{y}) \, ds . \blacksquare$$

For slowly varying parameters, these averages simply reduce to the original parameters. We assume that  $\bar{\varepsilon}(\mathbf{x})$ ,  $\bar{\sigma}^d(\mathbf{x})$  and  $\bar{\lambda}^d(\mathbf{x})$  have the same eigenvectors, or *principal axes*,  $\mathbf{r}_i$  ( $i = 1, 2, 3$ ). Let  $\bar{\varepsilon}_i$ ,  $\bar{\sigma}_i^d$ , and  $\bar{\lambda}_i^d$ , denote the corresponding eigenvalues of the averaged tensors. (Only two eigenvalues of  $\bar{\sigma}^d$  and one eigenvalue of  $\bar{\lambda}^d$  are possibly nonzero.) After some algebra, (4.3) gives

$$(4.4) \quad \frac{\varepsilon_i^{\text{eff}}}{\bar{\varepsilon}_i} = \left(1 - \frac{\xi_{0,i}}{d}\right) \left(1 + \frac{\bar{\lambda}_i^d}{i\omega\bar{\varepsilon}_i\xi_{0,i}d}\right),$$

for all directions  $\mathbf{r}_i$  with nonzero  $\bar{\sigma}_i^d$ , or  $\bar{\lambda}_i^d$ . Here, we define the *generalized plasmonic thickness* [23]

$$(4.5) \quad \xi_{0,i} = \frac{\bar{\sigma}_i^d}{2i\omega\bar{\varepsilon}_i} + \sqrt{\left(\frac{\bar{\sigma}_i^d}{2i\omega\bar{\varepsilon}_i}\right)^2 + \frac{\bar{\lambda}_i^d}{i\omega\bar{\varepsilon}_i}},$$

which accounts for the line conductivity. Evidently,  $\varepsilon_i^{\text{eff}} \simeq 0$  if the spacing,  $d$ , is close to the critical value  $d_c = \xi_{0,i}$  for some  $i$  and suitable ranges of values for  $\bar{\sigma}_i^d$  and  $\bar{\lambda}_i^d$  (e.g.,  $\text{Im}\bar{\sigma}_i^d > 0$ ,  $\text{Im}\bar{\lambda}_i^d > 0$ ).

We stress that for  $|\bar{\sigma}_i^d| \gg |\bar{\lambda}_i^d|$  (4.4) with (4.5) reduces to the known result

$$\frac{\varepsilon_i^{\text{eff}}}{\bar{\varepsilon}_i} \sim \left(1 - \frac{\xi_{0,i}}{d}\right), \quad \xi_{0,i} \approx \frac{\bar{\sigma}_i^d}{i\omega\bar{\varepsilon}_i},$$

which is also obtained via a Bloch-wave approach for planar sheets [23]. In contrast, if  $|\bar{\lambda}_i^d| \gg |\bar{\sigma}_i^d|$ , (4.4) reduces to

$$\frac{\varepsilon_i^{\text{eff}}}{\bar{\varepsilon}_i} \sim \left(1 - \frac{\xi_{0,i}}{d}\right), \quad \xi_{0,i} \approx \sqrt{\frac{\bar{\lambda}_i^d}{i\omega\bar{\varepsilon}_i}}.$$

Notice the distinctly different scaling of  $\xi_{0,i}$  with the conductivity parameter in this regime.

**4.3. On the physical role of corrector  $\chi$ .** Let us return to cell problem (3.2). We now provide a physical interpretation of its solution, the corrector  $\chi$ . In particular, we solve cell problem (3.2) for the three prototypical configurations shown in Figure 2 (see also Section 4.4.1). In all three geometries, we set the permittivity and surface conductivity equal to nonzero constants,  $\varepsilon(\mathbf{x}, \mathbf{y}) = \varepsilon$ ,  $\sigma(\mathbf{x}, \mathbf{y}) = \sigma$ , while we take  $\lambda(\mathbf{x}, \mathbf{y}) = 0$ . By the discussion in Section 4.4.1, we conclude that for the geometry of planar sheets with no edges (Figure 2(a))  $\chi \equiv 0$ . For the geometry of nanoribbons (Figure 2(b)),  $\chi_2 \equiv \chi_3 \equiv 0$ . The remaining geometry (Figure 2(c)) has only one vanishing corrector component,  $\chi_3 \equiv 0$ . The real and imaginary parts of the nontrivial corrector component  $\chi_1$  for the last two geometries are shown in Figure 3. The SPP excited by the edge discontinuity is evident in these settings; cf. [21].

Motivated by these numerical results, we develop an argument that the corrector,  $\chi$ , encodes the microscale response of the system to the macroscopic electromagnetic field,  $(\mathcal{E}(\mathbf{x}), \mathcal{H}(\mathbf{x}))$ . We start by noting that our scalings  $\sigma^d(\mathbf{x}) = d\sigma(\mathbf{x}, \mathbf{x}/d)$  and  $\lambda^d(\mathbf{x}) = d^2\lambda(\mathbf{x}, \mathbf{x}/d)$  imply that the typical length scales of surface and line waves (such as SPPs and EPPs) scale with  $d$  and  $d^2$ , respectively. Accordingly, we can identify the forcing in cell problem (3.2) due to  $\mathbf{e}_j$ . This forcing corresponds to a (normalized) asymptotically slow planar wave. In this sense, the cell problem describes the *local response of the microstructure* to all possible excitations by local plane waves.

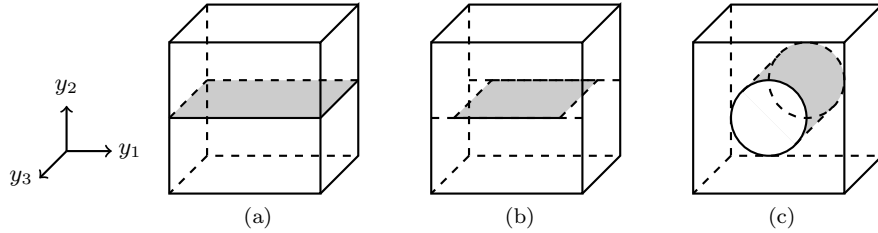


Fig. 2: Prototypical examples of microscopic geometries with conducting sheets for cell problem (3.2). (a) Infinite planar sheet, with no edges. (b) Planar strip (nanoribbon). (c) Sheet forming circular cylinder (nanotube). The corrector,  $\chi$ , can be characterized as follows: (a)  $\chi \equiv 0$ ; (b)  $\chi_2 = \chi_3 \equiv 0$  while  $\chi_1$  is nontrivial; and (c)  $\chi_3 \equiv 0$  while  $\chi_1$  and  $\chi_2$  are nontrivial.

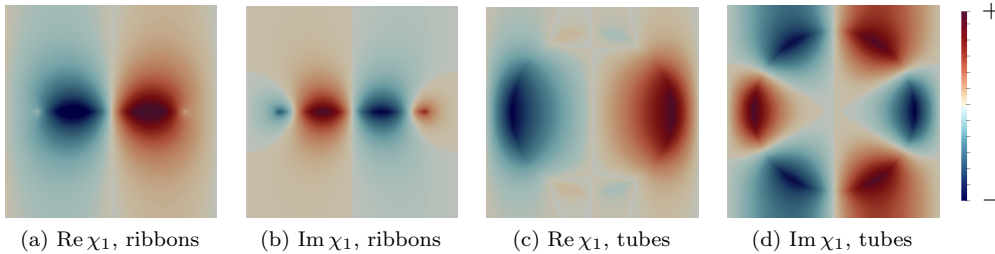


Fig. 3: Real and imaginary parts of corrector component  $\chi_1$  for geometries of Figures 2b,c in  $y_1y_2$ -plane. It is evident that internal edges in nanoribbons and curvature in nanotubes create SPPs.

This interpretation has an important consequence in light of the discussion in Section 4.4.1: All cases of vanishing correctors are indeed characterized by conditions (4.2). In fact, conditions (4.2) characterize exactly all microscale geometries that *do not permit* the excitation of SPPs by plane waves.

**5. Computational platform and examples of effective permittivity.** In this section, we introduce a computational platform that serves as a foundation for investigating the effective optical response of (sufficiently general) microscopic geometries. We implement the computational framework with the help of the finite element toolkit deal.II [4] and demonstrate its effectiveness on a prototypical and somewhat realistic example of a plasmonic crystal consisting of corrugated graphene sheets. In addition, we present a number of computational results concerning the frequency response of effective permittivity (3.4) by use of cell problem (3.2) for the geometries of nanoribbons and nanotubes (Figure 2b,c).

**5.1. Computational framework.** Building on computational methods that we developed for plasmonic problems [20, 21], we propose the following computational approach. We present approximations for solution  $\{\mathcal{E}, \mathcal{H}\}$  of homogenized problem (3.3) by use of an adaptive finite element scheme. Typically, for such a scheme to be efficient there is a need for advanced computational techniques, such

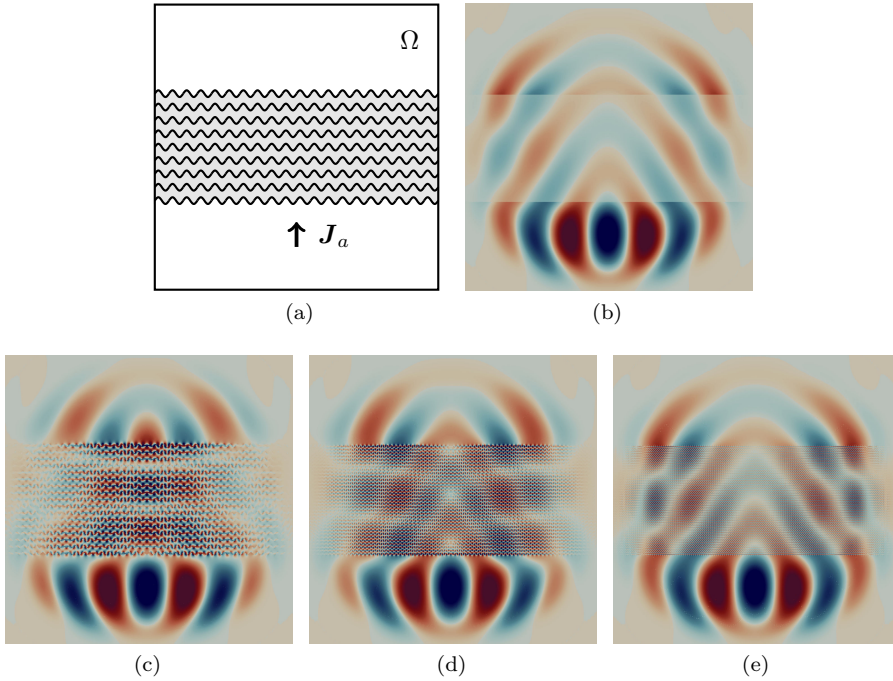


Fig. 4: (a) Geometry of a plasmonic-crystal slab of height 1 with corrugated layers of 2D material, where the corrugation is sinusoidal and the period is equal to the spacing,  $d$  (in the schematic  $d = 2^{-3}$ ). (b) Real part of electric field in the  $y$ -direction in the corresponding homogenization limit (as  $d \rightarrow 0$ ), via solution of cell problem (3.2) and computation of the homogenized solution given by (3.3). (c-e) Real part of electric field in the  $y$ -direction, based on direct numerical simulations of (2.1)–(2.3) (see [20]), for decreasing spacing,  $d$  (i. e., increasing degree of scale separation): (c)  $d = 2^{-4}$ ; (d)  $d = 2^{-5}$ ; (e)  $d = 2^{-6}$ .

as the construction of a *perfectly matched layer* for treatment of absorbing boundary conditions, and strategies for adaptive local refinement of meshes. We refer the reader to [20] for details.

- During the finite element computation of (3.3) we *reconstruct* the effective permittivity tensor  $\varepsilon^{\text{eff}}$  when needed by first approximating the corrector  $\chi_i$  ( $i = 1, 2, 3$ ) that is described by cell problem (3.2), and subsequently evaluating (3.4) with a suitable numerical quadrature rule. This is done with the same

finite element toolkit [4] that we use for effective problem (3.3). We make the remark that using a finite element discretization is particularly advantageous for approximating cell problem (3.2) that contains a jump condition over smooth, curved hypersurfaces. For the sake of brevity we omit algorithmic details but refer the reader to [22] for a discussion of the variational form of equations (3.3) and (3.2), as well as to [4] for algorithmic details on curved boundary approximations, numerical quadrature, and numerical linear algebra.

We demonstrate the applicability of our computational platform by use of a prototypical scattering configuration. It consists of a dipole situated in close proximity to a plasmonic crystal (slab) of height 1 consisting of many layers of corrugated 2D

sheets at distance  $d$ ; see Figure 4. The sheet corrugation is described by a sine curve of amplitude  $d/4$  and period  $d$  (Figure 4a). The computational result of our proposed scheme involving the homogenized system is shown in Figure 4b. In addition, Figures 4c-e show the results of a direct numerical simulation of the electric field  $\mathbf{E}$  described by (2.1) and (2.2) for an increasing level of scale separation ( $d = 2^{-4}, 2^{-5}, 2^{-6}$ , respectively). The direct numerical computations shown in Figure 4b-d require a very fine resolution that results in linear systems with up to  $1.6 \times 10^7$  unknowns. In contrast, our proposed computational framework can be efficiently implemented by use of a moderate resolution in the approximation scheme of around  $3.2 \times 10^4$  unknowns, a number smaller by a factor of about 500 than the one for the direct numerical simulation. This comparison demonstrates that already for a moderate scale separation of  $d = 2^{-6}$ , the computational platform leads to a significant saving of computational resources.

Our example demonstrates in addition that the predictive quality of the homogenized solution improves with increasing scale separation: Typically, we have a good agreement between the electromagnetic field  $\{\mathbf{E}, \mathbf{H}\}$  that is described system (2.1) and (2.2) and the homogenized field  $\{\mathcal{E}, \mathcal{H}\}$  given by (3.3) for a scale separation of  $d \approx 1/64$  and less, even for scattering configuration with dominant near field character as shown in Figure 4. In general, the upper limit of  $d$  for which the homogenized system (3.3) has some predictive quality heavily depends on the geometry and the location of sources.

We should add the remark that our homogenization result remains valid also for current-carrying sources,  $\mathbf{J}_a$ , situated inside the geometry provided the function  $\mathbf{J}_a(\mathbf{x})$  is square integrable. This claim would typically require that dipole sources have to be regularized, as in our computational example. In the case with (perfect, unregularized) point sources the emerging near field might not be captured in its entirety by our computational framework.

**5.2. Effective permittivity tensors in prototypical geometries.** In order to relate numerical results obtained by solving cell problem (3.2) to the averaging in (3.4) and compute physical quantities as a function of frequency,  $\omega$ , it is necessary to use a suitable model for the material parameters. If  $\lambda^d = 0$ , the only modeling parameters that enter (3.2) are  $\varepsilon(\mathbf{x}, \mathbf{y})$  and  $\frac{1}{i\omega}\sigma(\mathbf{x}, \mathbf{y})$ . We assume that  $\varepsilon(\mathbf{x}, \mathbf{y}) = \varepsilon$  is constant and that the tangential parts of  $\sigma(\mathbf{x}, \mathbf{y}) = \sigma(\mathbf{y})$  are given by spatially constant values. Thus, the only microscale ( $\mathbf{y}$ -) parameter dependence to be accounted for is the one in  $\frac{1}{i\omega}\sigma(\mathbf{x}, \mathbf{y})$ ; cf. Figure 2 for geometries of interest.

The surface conductivity,  $\sigma^d$ , of doped graphene can plausibly be described by the Kubo formula, which takes into account electronic excitations and temperature effects [6]. However, in a suitable parameter regime that includes terahertz frequencies, in which fine-scale SPPs on graphene can typically be generated, it has been shown that the Kubo formula reduces to the (much simpler) Drude model [10]. By this model, the tangential components of a spatially constant  $\sigma^d$  are given by the formula

$$\sigma^d = \frac{i e^2 E_F}{\varepsilon_0 \pi \hbar^2 (\omega + i/\tau)} .$$

Here,  $e$  is the electron charge,  $\hbar$  denotes the (reduced) Planck constant,  $\varepsilon_0$  is the vacuum permittivity,  $E_F$  denotes the Fermi energy, and  $\tau$  is the electronic relaxation time. In this context, an  $\mathbf{x}$ -dependence of  $\sigma^d$  may arise from spatial variations of the parameters  $E_F$  and  $\tau$ .

We proceed to carry out numerical computations for  $\varepsilon_{ij}^{\text{eff}}$ . Using typical parameter



values for graphene [6], we set  $\tau = 0.5 \cdot 10^{-12}$  s and apply the following rescalings:  $E_F = \tilde{E}_F \cdot 10^{-19}$  J,  $\omega = \tilde{\omega} \cdot 10^{14}$  Hz,  $d = \tilde{d} \cdot 10$  nm, with  $0 \leq \tilde{E}_F \leq 1.6$ ,  $0.5 \leq \tilde{\omega} \leq 4.0$ , and  $0 \leq \tilde{d} \leq 20.0$ . The surface average in (3.4) of the effective permittivity tensor,  $\varepsilon^{\text{eff}}$ , has the constant ( $\mathbf{y}$ -independent) prefactor

$$(5.1) \quad \eta := \frac{1}{i\omega} \sigma = \frac{1}{i\omega d} \sigma^d = 82.9 \frac{\tilde{E}_F}{\tilde{d} \tilde{\omega} (\tilde{\omega} + 0.02i)}.$$

Utilizing definition (5.1) we conveniently express the matrix elements of  $\varepsilon^{\text{eff}}$  given in (3.4) as

$$\frac{\varepsilon_{ij}^{\text{eff}}}{\varepsilon} = 1 - \frac{\eta}{\varepsilon} \int_{\Sigma} P_t(\mathbf{y}) (\mathbf{e}_j + \nabla_y \chi_j(\mathbf{x}, \mathbf{y})) \cdot \mathbf{e}_i \, d\mathbf{o}_y.$$

Here,  $P_t(\mathbf{y})$  denotes the projection onto the tangential space of  $\Sigma^d$  at point  $\mathbf{y}$ . This formula for  $\varepsilon_{ij}^{\text{eff}}$  uncovers an important property: Up to a factor of  $\varepsilon$ , computational results for the cell problem only depend on the ratio  $\eta/\varepsilon$ . Thus, it is sufficient to compute values for  $\varepsilon_{ij}^{\text{eff}}$  by setting  $\varepsilon = 1$ .

Let us now recall the discussion about vanishing correctors in Sections 4.4.1, 4.3. For the prototypical geometries of Figure 2, the respective effective permittivities have the matrix forms:

$$(5.2) \quad \varepsilon_S^{\text{eff}} = \begin{pmatrix} \varepsilon_{11}^S & 0 & 0 \\ 0 & \varepsilon & 0 \\ 0 & 0 & \varepsilon_{33}^S \end{pmatrix}, \quad \varepsilon_R^{\text{eff}} = \begin{pmatrix} \varepsilon_{11}^R & 0 & 0 \\ 0 & \varepsilon & 0 \\ 0 & 0 & \varepsilon_{33}^R \end{pmatrix}, \quad \varepsilon_T^{\text{eff}} = \begin{pmatrix} \varepsilon_{11}^T & 0 & 0 \\ 0 & \varepsilon_{22}^T & 0 \\ 0 & 0 & \varepsilon_{33}^T \end{pmatrix}.$$

Here, the subscript (S, R or T) for each matrix indicates the type of geometry: S corresponds to the geometry with planar sheets and no edges (Figure 2a); R stands for the nanoribbons geometry (Figure 2b); and T corresponds to the nanotubes geometry (Figure 2c). Due to vanishing corrector components, the matrix element  $\varepsilon_{11}^S$  is given in closed form by (4.3), viz.,

$$(5.3) \quad \varepsilon_{11}^S = 1 - \eta; \quad \varepsilon_{11}^S = \varepsilon_{33}^S = \varepsilon_{33}^R = \varepsilon_{33}^T.$$

In the remaining numerical computations, we focus on the more complicated geometries with nanoribbons and nanotubes (Figure 2b,c). To determine  $\varepsilon_{11}^R$  and  $\varepsilon_{11}^T = \varepsilon_{22}^T$ , we solve cell problem (3.2) directly and compute the average by (3.4). The computations are carried out by the finite element toolkit deal.II [4]. To this end, we sample over the frequency range  $0.5 \leq \tilde{\omega} \leq 4.0$  with the choice  $\tilde{E}_F = 1$  and  $\tilde{d} = 20.72$ . The real and imaginary parts of  $\varepsilon_{11}^R$  and  $\varepsilon_{11}^T$  are plotted as a function of frequency in Figures 5a, b. The real and imaginary parts of this  $\varepsilon$  satisfy the Kramers-Kronig relations. We observe that each of these functions exhibits a strong Lorentzian resonance at around  $(\varepsilon_{11}^R:)$   $\tilde{\omega}_R = 2.25002(2)$ , and  $(\varepsilon_{11}^T:)$   $\tilde{\omega}_R = 1.70285(3)$ . It is of interest to note that the ENZ effect occurs at the following (rescaled) frequencies:  $(\varepsilon_{11}^R:)$   $\tilde{\omega} \approx 2.752$ ,  $(\varepsilon_{11}^T:)$   $\tilde{\omega} \approx 2.755$ . Here, both frequencies are determined by interpolating the computational results displayed in Figure 5 (obtained via the solution of cell problem (3.2) with a finite element method) with a Lorentzian function. Note that (5.3) implies the critical frequency  $\tilde{\omega} \approx 2$  for  $\varepsilon_{11}^S$  where  $\varepsilon_{11}^S = \varepsilon_{33}^S = \varepsilon_{33}^R = \varepsilon_{33}^T$ .

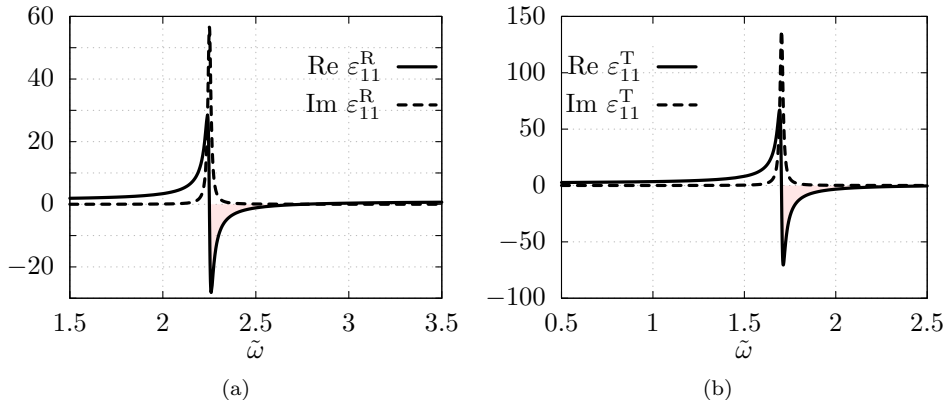


Fig. 5: Plots of real and imaginary parts of matrix elements of  $\varepsilon^{\text{eff}}$  as a function of frequency by (5.2) for the geometries of Figures 2b, c. (a)  $\varepsilon_{11}^{\text{R}}$  for nanoribbons; and (b)  $\varepsilon_{11}^{\text{T}}$  or  $\varepsilon_{22}^{\text{T}}$  ( $\varepsilon_{11}^{\text{T}} = \varepsilon_{22}^{\text{T}}$ ) for nanotubes. The shaded area indicates the frequency regime for negative real part in each case.

**6. Conclusion.** In this paper, we carried out a formal asymptotic analysis to homogenize time-harmonic Maxwell's equations in plasmonic crystals made of conducting sheets with microscale spacing  $d$ , in the limit as  $d \rightarrow 0$  via suitable scalings of material parameters. The homogenized system features an effective permittivity tensor,  $\varepsilon^{\text{eff}}$ , given by an averaging procedure that involves a weighted volume average of the bulk permittivity, as well as a weighted surface average of the surface conductivity,  $\sigma^d$ , and a weighted line average of the line charge density,  $\lambda^d$ , of the sheets. The vector-valued corrector field of this procedure solves a closed cell problem. We showed analytically how the combination of the complex-valued  $\sigma^d$  and  $\lambda^d$  yields an ENZ effect; and defined the related critical spacing which depends on  $\sigma^d$  and  $\lambda^d$ .

The introduction of the line charge density,  $\lambda^d$ , in our microscale model and homogenization procedure is an aspect that deserves particular emphasis. We believe that this feature has eluded previous works in plasmonics. In fact, a general and precise quantitative description of the influence of the physics at material edges on effective optical parameters of plasmonic crystals made of 2D materials is a largely open problem. Edge effects have received significant attention recently because of observations of EPPs [15, 11]. Our discussion of a homogenization procedure involving a line charge density on material edges contributes to this effort. For example, we demonstrated that the (generalized) plasmonic thickness has an algebraic dependence on the line charge density different from that on the surface conductivity of the 2D material. In addition, our formalism suggests a few mathematical problems (regarding the well-posedness and formal proof of homogenization results) which were not addressed here.

We also discussed how our homogenization result can be incorporated into well established computational approaches for time harmonic Maxwell equations. This procedure involves the computation of effective material parameters by approximation of the solution of the corresponding cell problems and averaging. We demonstrated the feasibility of this approach in a geometry with corrugated sheets; and computed the Lorentz-type resonance of two prototypical microscopic geometries. The computational framework that we introduced paves the road for future, systematic computational

investigations of complicated design problems in the plasmonics of 2D materials [28, 18, 26].

Our results have a few limitations and point to open problems in asymptotics. For instance, the asymptotic analysis is based on a strong periodicity assumption. Further, we do not discuss boundary layers in the homogenization procedure due to the interaction of the microstructure with boundaries of the (scattering) domain. It is also worth mentioning that scaling assumptions different from the ones chosen here may lead to different homogenization results.

### Appendix A. Two-scale expansion and asymptotics.

In this appendix, we carry out in detail the asymptotic analysis that was outlined in Section 3. As a first step, we apply the two-scale asymptotic expansion to (2.1) and (2.2). By collecting all terms of the order of  $d^{-1}$  in region  $\Omega \times Y$  and of the order of  $d^0$  on  $\Omega \times \Sigma$ , we obtain the equations

$$(A.1) \quad \begin{cases} \nabla_y \times \mathbf{E}^{(0)} = 0, & \nabla_y \times \mathbf{H}^{(0)} = 0, \\ \nabla_y \cdot (\varepsilon \mathbf{E}^{(0)}) = 0, & \nabla_y \cdot \mathbf{H}^{(0)} = 0; \\ \left[ \boldsymbol{\nu} \times \mathbf{E}^{(0)} \right]_{\Sigma} = 0, & \left[ \boldsymbol{\nu} \times \mathbf{H}^{(0)} \right]_{\Sigma} = 0, \\ \left[ \boldsymbol{\nu} \cdot (\varepsilon \mathbf{E}^{(0)}) \right]_{\Sigma} = \frac{1}{i\omega} \nabla_y \cdot (\sigma \mathbf{E}^{(0)}), & \left[ \boldsymbol{\nu} \cdot \mathbf{H}^{(0)} \right]_{\Sigma} = 0. \end{cases}$$

In a similar vein, a second set of equations is obtained by collecting all terms of the order of  $d^0$  in  $\Omega \times Y$  and of the order of  $d^1$  on  $\Omega \times \Sigma$ , viz.,

$$(A.2) \quad \begin{cases} \nabla_x \times \mathbf{H}^{(0)} + \nabla_y \times \mathbf{H}^{(1)} = -i\omega \varepsilon \mathbf{E}^{(0)} + \mathbf{J}_a, \\ \nabla_x \times \mathbf{E}^{(0)} + \nabla_y \times \mathbf{E}^{(1)} = i\omega \mu_0 \mathbf{H}^{(0)}, \\ \nabla_x \cdot (\varepsilon \mathbf{E}^{(0)}) + \nabla_y \cdot (\varepsilon \mathbf{E}^{(1)}) = \frac{1}{i\omega} \nabla_x \cdot \mathbf{J}_a, \\ \nabla_x \cdot \mathbf{H}^{(0)} + \nabla_y \cdot \mathbf{H}^{(1)} = 0, \end{cases}$$

and

$$(A.3) \quad \begin{cases} \left[ \boldsymbol{\nu} \times \mathbf{E}^{(1)} \right]_{\Sigma} = 0, & \left[ \boldsymbol{\nu} \times \mathbf{H}^{(1)} \right]_{\Sigma} = \sigma \mathbf{E}^{(0)}, \\ \left[ \boldsymbol{\nu} \cdot (\varepsilon \mathbf{E}^{(1)}) \right]_{\Sigma} = \frac{1}{i\omega} (\nabla_x \cdot (\sigma \mathbf{E}^{(0)}) + \nabla_y \cdot (\sigma \mathbf{E}^{(1)})), & \left[ \boldsymbol{\nu} \cdot \mathbf{H}^{(1)} \right]_{\Sigma} = 0. \end{cases}$$

In (A.1)–(A.3), the differential equations are valid for  $(\mathbf{x}, \mathbf{y}) \in \Omega \times Y$ ; while the jump conditions hold for  $(\mathbf{x}, \mathbf{y}) \in \Omega \times \Sigma$ .

So far, we used boundary conditions on the interior of the sheets,  $\Sigma^d \cap \Omega \setminus \partial \Sigma^d$ . We now focus on (2.3), imposed on the edges,  $\partial \Sigma^d \cap \Omega$ . First, we introduce the rescaled jump  $\{ \cdot \}_{\partial \Sigma}$  in a way analogous to definition (2.4) for the jump  $\{ \cdot \}_{\partial \Sigma^d}$ , viz.,

$$\{ \mathbf{F} \}_{\partial \Sigma}(\mathbf{x}, \mathbf{y}) := \lim_{\alpha \searrow 0} \int_{-\alpha}^{\alpha} (\mathbf{F}(\mathbf{x}, \mathbf{y} + \alpha^2 \mathbf{n} + \zeta \boldsymbol{\nu}) - \mathbf{F}(\mathbf{x}, \mathbf{y} - \alpha^2 \mathbf{n} + \zeta \boldsymbol{\nu})) d\zeta \quad \mathbf{y} \in \partial \Sigma \quad \blacksquare$$

By carrying out the leading-order asymptotic expansion for the singular jump of (2.4), we see that  $\{ \cdot \}_{\partial \Sigma^d} \rightarrow d \{ \cdot \}_{\partial \Sigma}$ . Consequently, the first condition of (2.3) is expanded to

$$(A.4) \quad \left\{ \mathbf{n} \times \mathbf{H}^{(1)} \right\}_{\partial \Sigma} = \lambda \mathbf{E}^{(0)} \quad \text{on } \Omega \times (\partial \Sigma \setminus \partial Y).$$

Furthermore, the expansion of the second one of conditions (2.3) results in the following boundary conditions to the two lowest orders in  $d$ :

$$(A.5) \quad \mathbf{n} \cdot (\sigma \mathbf{E}^{(0)}) = \nabla_y \cdot (\lambda \mathbf{E}^{(0)}), \quad \mathbf{n} \cdot (\sigma \mathbf{E}^{(1)}) = \nabla_x \cdot (\lambda \mathbf{E}^{(0)}) + \nabla_y \cdot (\lambda \mathbf{E}^{(1)}),$$

which hold on  $\Omega \times (\partial\Sigma \setminus \partial Y)$ .

**A.1. Characterization of  $\mathbf{E}^{(0)}$  and  $\mathbf{H}^{(0)}$ .** We now use (A.1) to characterize  $\mathbf{E}^{(0)}(\mathbf{x}, \mathbf{y})$  and  $\mathbf{H}^{(0)}(\mathbf{x}, \mathbf{y})$  in more detail. Since a conservative periodic vector field is the sum of a constant vector and the gradient of a periodic function (potential), we can write the general solution to the first equation of (A.1) as

$$(A.6) \quad \mathbf{E}^{(0)}(\mathbf{x}, \mathbf{y}) = \mathcal{E}(\mathbf{x}) + \nabla_y \varphi(\mathbf{x}, \mathbf{y}), \quad \varphi(\mathbf{x}, \mathbf{y}) = \sum_j \chi_j(\mathbf{x}, \mathbf{y}) \mathcal{E}_j(\mathbf{x}).$$

In this vein, a conservative and divergence-free periodic vector field must be constant. Hence, the general solution to the second and fourth laws of the first group of equations in (A.1) is given by

$$(A.7) \quad \mathbf{H}^{(0)}(\mathbf{x}, \mathbf{y}) = \mathcal{H}(\mathbf{x}).$$

The functions  $\mathcal{E}(\mathbf{x})$ ,  $\mathcal{H}(\mathbf{x})$  and  $\chi_j(\mathbf{x}, \mathbf{y})$  ( $j = 1, 2, 3$ ) are further characterized below.

**A.2. Derivation of cell problem.** Next, we derive a closed set of equations that fully describe the functions  $\chi_j(\mathbf{x}, \mathbf{y})$  introduced in (A.6). These equations comprise the cell problem accounting for the microstructure details.

First, we substitute (A.6) into the respective, zeroth-order expressions in (A.1) and (A.5). Specifically, we use the third law of the first group of equations in (A.1); the first and third jump conditions in (A.1); and the first condition in (A.5). Thus, we obtain the following equations:

$$\left\{ \begin{array}{l} \sum_j \nabla_y \cdot (\varepsilon(\mathbf{x}, \mathbf{y})(\mathbf{e}_j + \nabla_y \chi_j(\mathbf{x}, \mathbf{y}))) \mathcal{E}_j(\mathbf{x}) = 0 \quad \text{in } \Omega \times Y, \\ \sum_j \left[ \boldsymbol{\nu} \times (\varepsilon(\mathbf{x}, \mathbf{y})(\mathbf{e}_j + \nabla_y \chi_j(\mathbf{x}, \mathbf{y}))) \right]_{\Sigma} \mathcal{E}_j(\mathbf{x}) = 0 \quad \text{on } \Omega \times \Sigma, \\ \sum_j \left[ \boldsymbol{\nu} \cdot (\varepsilon(\mathbf{x}, \mathbf{y})(\mathbf{e}_j + \nabla_y \chi_j(\mathbf{x}, \mathbf{y}))) \right]_{\Sigma} \mathcal{E}_j(\mathbf{x}) = \\ \qquad \qquad \qquad \frac{1}{i\omega} \sum_j \nabla_y \cdot (\sigma(\mathbf{x}, \mathbf{y})(\mathbf{e}_j + \nabla_y \chi_j(\mathbf{x}, \mathbf{y}))) \mathcal{E}_j(\mathbf{x}) \quad \text{on } \Omega \times \Sigma, \\ \sum_j \mathbf{n} \cdot (\sigma(\mathbf{x}, \mathbf{y})(\mathbf{e}_j + \nabla_y \chi_j(\mathbf{x}, \mathbf{y}))) \mathcal{E}_j(\mathbf{x}) = \\ \qquad \qquad \qquad \sum_j \nabla_y \cdot (\lambda(\mathbf{x}, \mathbf{y})(\mathbf{e}_j + \nabla_y \chi_j(\mathbf{x}, \mathbf{y}))) \mathcal{E}_j(\mathbf{x}) \quad \text{on } \Omega \times (\partial\Sigma \setminus \partial Y). \end{array} \right. \quad \blacksquare$$

Here,  $\mathcal{E}_j$  and  $\chi_j$  are coupled. To simplify this description, we treat each term containing  $\chi_j(\mathbf{x}, \mathbf{y})$ , which accounts for the microscale behavior of  $\mathbf{E}^{(0)}(\mathbf{x}, \mathbf{y})$ , as independent from  $\mathcal{E}_j(\mathbf{x})$  ( $j = 1, 2, 3$ ). Thus, the above equations decouple into three distinct problems, one for each  $\chi_j$ , as displayed in (3.2). Equations (3.2) along with the condition that  $\chi_j(\mathbf{x}, \cdot)$  be  $Y$ -periodic form the desired, closed cell problem. Notice that  $\mathbf{x}$  plays the role of a parameter. Hence, the above cell problem uniquely describes  $\chi_j(\mathbf{x}, \cdot)$  for any given (macroscopic) point  $\mathbf{x}$ .

**A.3. Homogenized macroscale problem.** Our remaining task is to derive corresponding macroscale equations for the functions  $\boldsymbol{\mathcal{E}}(\mathbf{x})$  and  $\boldsymbol{\mathcal{H}}(\mathbf{x})$ . We start by substituting (A.6) and (A.7) into the first equation of (A.2) and averaging (in cell  $Y$ ) over the fast variable,  $\mathbf{y}$ . Hence, we obtain the following expression:

$$(A.8) \quad \nabla_x \times \boldsymbol{\mathcal{H}}(\mathbf{x}) + \int_Y \nabla_y \times \mathbf{H}^{(1)}(\mathbf{x}, \mathbf{y}) \, d\mathbf{y} = \\ - i\omega \sum_j \int_Y \varepsilon(\mathbf{x}, \mathbf{y}) (\mathbf{e}_j + \nabla_y \chi_j(\mathbf{x}, \mathbf{y})) \, d\mathbf{y} \, \mathcal{E}_j(\mathbf{x}) + \mathbf{J}_a(\mathbf{x}) .$$

By use of the Gauss theorem and the  $Y$ -periodicity of  $\mathbf{H}^{(1)}$ , the second term on the left-hand side of the above equation is written as

$$\int_Y \nabla_y \times \mathbf{H}^{(1)} \, d\mathbf{y} = - \int_{\Sigma} [\boldsymbol{\nu} \times \mathbf{H}^{(1)}]_{\Sigma} \, d\mathbf{o}_y - \int_{\partial\Sigma \setminus \partial Y} \left\{ \mathbf{n} \times \mathbf{H}^{(1)} \right\}_{\partial\Sigma^d} \, d\mathbf{s} \\ = - \int_{\Sigma} \sigma(\mathbf{x}, \mathbf{y}) \mathbf{E}^{(0)} \, d\mathbf{o}_y - \int_{\partial\Sigma \setminus \partial Y} \lambda(\mathbf{x}, \mathbf{y}) \mathbf{E}^{(0)} \, d\mathbf{s} \\ = - \sum_j \left\{ \int_{\Sigma} \sigma(\mathbf{x}, \mathbf{y}) (\mathbf{e}_j + \nabla_y \chi_j) \, d\mathbf{o}_y + \int_{\partial\Sigma \setminus \partial Y} \lambda(\mathbf{x}, \mathbf{y}) (\mathbf{e}_j + \nabla_y \chi_j) \, d\mathbf{s} \right\} \mathcal{E}_j(\mathbf{x}) . \quad \blacksquare$$

In the above, the second equality comes from using the second jump condition of (A.3), and (A.4). The third equality follows from (A.6). Let us now define the *effective permittivity tensor*  $\varepsilon^{\text{eff}}$  by

$$(A.9) \quad \varepsilon_{ij}^{\text{eff}}(\mathbf{x}) := \int_Y \varepsilon(\mathbf{x}, \mathbf{y}) (\mathbf{e}_j + \nabla_y \chi_j(\mathbf{x}, \mathbf{y})) \cdot \mathbf{e}_i \, d\mathbf{y} - \frac{1}{i\omega} \int_{\Sigma} \sigma(\mathbf{x}, \mathbf{y}) (\mathbf{e}_j + \nabla_y \chi_j(\mathbf{x}, \mathbf{y})) \cdot \mathbf{e}_i \, d\mathbf{o}_y \\ - \frac{1}{i\omega} \int_{\partial\Sigma \setminus \partial Y} \lambda(\mathbf{x}, \mathbf{y}) (\mathbf{e}_j + \nabla_y \chi_j(\mathbf{x}, \mathbf{y})) \cdot \mathbf{e}_i \, d\mathbf{s} .$$

In view of this definition of  $\varepsilon^{\text{eff}}$ , (A.8) takes the form

$$\nabla \times \boldsymbol{\mathcal{H}} = -i\omega \varepsilon^{\text{eff}} \boldsymbol{\mathcal{E}} + \mathbf{J}_a ,$$

which describes the effective Ampère-Maxwell law.

The last three equations of (A.2) can be manipulated in a similar fashion. For example, consider the third equation. By using (A.6) and (A.7) and averaging over the fast variable,  $\mathbf{y}$ , we obtain

$$(A.10) \quad \nabla_x \cdot \left( \sum_j \int_Y \varepsilon(\mathbf{x}, \mathbf{y}) (\mathbf{e}_j + \nabla_y \chi_j(\mathbf{x}, \mathbf{y})) \, d\mathbf{y} \, \mathcal{E}_j(\mathbf{x}) \right) \\ + \int_Y \nabla_y \cdot (\varepsilon(\mathbf{x}, \mathbf{y}) \mathbf{E}^{(1)}(\mathbf{x}, \mathbf{y})) \, d\mathbf{y} = \frac{1}{i\omega} \nabla_x \cdot \mathbf{J}_a(\mathbf{x}) .$$

Next, we manipulate the second term of the left-hand side by applying the Gauss

theorem and utilizing the second jump condition of (A.3), as follows:

$$\begin{aligned}
\int_Y \nabla_y \cdot (\varepsilon \mathbf{E}^{(1)}) dy &= - \int_{\Sigma} [\nu \cdot (\varepsilon \mathbf{E}^{(1)})]_{\Sigma} do_y \\
&= - \int_{\Sigma} \frac{1}{i\omega} (\nabla_x \cdot (\sigma \mathbf{E}^{(0)}) + \nabla_y \cdot (\sigma \mathbf{E}^{(1)})) do_y \\
&= - \frac{1}{i\omega} \nabla_x \cdot \left( \sum_j \int_{\Sigma} \sigma(\mathbf{x}, \mathbf{y}) (\mathbf{e}_j + \nabla_y \chi_j(\mathbf{x}, \mathbf{y})) do_y \mathcal{E}_j(\mathbf{x}) do_y \right) \\
&\quad - \frac{1}{i\omega} \int_{\Sigma} \nabla_y \cdot (\sigma \mathbf{E}^{(1)}) do_y. \blacksquare
\end{aligned}$$

By applying the Gauss theorem and utilizing the second boundary condition in (A.5), we find

$$\begin{aligned}
\int_{\Sigma} \nabla_y \cdot (\sigma \mathbf{E}^{(1)}) do_y &= \int_{\partial \Sigma} \mathbf{n} \cdot (\sigma \mathbf{E}^{(1)}) ds = \int_{\partial \Sigma \setminus \partial Y} \mathbf{n} \cdot (\sigma \mathbf{E}^{(1)}) ds \\
&= \int_{\partial \Sigma \setminus \partial Y} \nabla_x \cdot (\lambda \mathbf{E}^0) + \nabla_y \cdot (\lambda \mathbf{E}^1) ds \\
&= \nabla_x \cdot \left( \sum_j \int_{\partial \Sigma \setminus \partial Y} \lambda(\mathbf{x}, \mathbf{y}) (\mathbf{e}_j + \nabla_y \chi_j(\mathbf{x}, \mathbf{y})) ds \mathcal{E}_j(\mathbf{x}) \right).
\end{aligned}$$

The second equality (exclusion of  $\partial Y$ ) exploits the fact that  $\sigma \mathbf{E}^{(1)}(\mathbf{x}, \cdot)$  is  $Y$ -periodic and, thus, single valued on  $\partial \Sigma \cap \partial Y$ . Notice, however, that the normal vector  $\mathbf{n}$  changes sign. The last integral in the second line vanishes because  $\partial \Sigma \setminus Y$  has no boundary. Substituting the result of these manipulations into (A.10) and utilizing (A.9), we obtain

$$\nabla \cdot (\varepsilon^{\text{eff}} \mathcal{E}) = \frac{1}{i\omega} \nabla \cdot \mathbf{J}_a.$$

Similar steps can be applied to the remaining equations of (A.2). The homogenized system finally reads

$$(A.11) \quad \begin{cases} \nabla \times \mathcal{E} = i\omega \mu_0 \mathcal{H}, & \nabla \times \mathcal{H} = -i\omega \varepsilon^{\text{eff}} \mathcal{E} + \mathbf{J}_a; \\ \nabla \cdot (\varepsilon^{\text{eff}} \mathcal{E}) = \frac{1}{i\omega} \nabla \cdot \mathbf{J}_a, & \nabla \cdot \mathcal{H} = 0. \end{cases}$$

### Appendix B. Derivation of compatibility conditions from Gauss' and Ampère's law.

In this section, we give a short derivation of the internal compatibility condition (2.3).

For an arbitrary volume  $V$  in  $\Omega$ , the integral over the *electric displacement in normal direction* has to be equal to the integral over the total charge density contained in  $V$ ,

$$i\omega \int_V \rho dx = \int_{\partial V} \mathbf{n}_{\partial V} \cdot (\varepsilon^d \mathbf{E}^d) do_x.$$

We now choose  $V$  to be an arbitrary rectangular box containing a part of the edge  $\partial \Sigma^d$ . We extend the sheet over the edge parallel in  $\mathbf{n}$ -direction, and assume  $\sigma^d = 0$

in the extension. The box shall be of vanishing length and height, and with top and bottom faces parallel to the extended sheet  $\Sigma_*^d$ ; see Figure 6. Then,

$$\begin{aligned} \lim_{\text{height} \rightarrow 0} i\omega \int_V \rho \, dx &= \lim_{\text{height} \rightarrow 0} \int_{\partial V} \mathbf{n}_{\partial V} \cdot (\varepsilon^d \mathbf{E}^d) \, do_x \\ &= \lim_{\text{height} \rightarrow 0} \int_{\text{top}} \boldsymbol{\nu} \cdot (\varepsilon^d \mathbf{E}^d)^{\text{above}} \, do_x - \int_{\text{bottom}} \boldsymbol{\nu} \cdot (\varepsilon^d \mathbf{E}^d)^{\text{below}} \, do_x \\ &= + \int_{V \cap \Sigma_*^d} \boldsymbol{\nu} \cdot (\varepsilon^d \mathbf{E}^d)^{\text{above}} \, do_x - \int_{V \cap \Sigma_*^d} \boldsymbol{\nu} \cdot (\varepsilon^d \mathbf{E}^d)^{\text{below}} \, do_x. \end{aligned}$$

Here,  $\mathbf{n}_{\partial V}$  denotes the outward pointing unit normal on faces of the volume  $V$  and  $\boldsymbol{\nu}$  is the normal field on  $\Sigma_*^d$ . Now, utilizing the third jump condition in (2.2) we conclude that

$$\begin{aligned} \lim_{\text{height} \rightarrow 0} i\omega \int_V \rho \, dx &= \int_{V \cap \Sigma_*^d} [\boldsymbol{\nu} \cdot (\varepsilon^d \mathbf{E}^d)]_{\Sigma^d} \, do_x \\ &= \int_{V \cap \Sigma_*^d} \nabla \cdot (\sigma^d \mathbf{E}^d) \, do_x \\ &= \int_{\partial V \cap \Sigma_*^d} \mathbf{n} \cdot (\sigma^d \mathbf{E}^d) \, do_x. \end{aligned}$$

Here,  $\mathbf{n}$  is the outward pointing normal on the edge, see Figure 6. By keeping the width (dimension parallel to the edge  $\partial\Sigma^d$ ) fixed and in the limit of vanishing height and length, we conclude that the volume integral over the charge density  $\rho$  reduces to

$$\lim_{\text{height} \rightarrow 0} \lim_{\text{length} \rightarrow 0} i\omega \int_V \rho \, dx = \int_{V \cap \partial\Sigma^d} \nabla \cdot (\lambda^d(\mathbf{x}) \mathbf{E}^d(\mathbf{x})) \, ds.$$

Consequently,

$$\int_{V \cap \partial\Sigma^d} \nabla \cdot (\lambda^d(\mathbf{x}) \mathbf{E}^d(\mathbf{x})) \, ds = \int_{V \cap \partial\Sigma^d} [\mathbf{n} \cdot (\sigma^d \mathbf{E}^d)]_{\Sigma^d} \, do_x.$$

Due to the fact that  $V$  was chosen arbitrarily, we conclude that

$$[\mathbf{n} \cdot (\sigma^d \mathbf{E}^d)]_{\Sigma^d} = \nabla \cdot (\lambda^d(\mathbf{x}) \mathbf{E}^d(\mathbf{x}))$$

has to hold true pointwise on  $\partial\Sigma^d$ . But  $\sigma^d$  vanishes outside of  $\Sigma^d$ , thus

$$\mathbf{n} \cdot (\sigma^d \mathbf{E}^d) = \nabla \cdot (\lambda^d(\mathbf{x}) \mathbf{E}^d(\mathbf{x})) \quad \text{on } \partial\Sigma^d.$$

In a similar vain, let  $A$  be an arbitrary area element perpendicular to the edge; see Figure 7. By virtue of Ampère's law we have

$$(B.1) \quad \int_{\partial A} \mathbf{H}^d \cdot d\mathbf{s} = \int_A \mathbf{J} \cdot \boldsymbol{\tau} \, do_x,$$

where  $\boldsymbol{\tau}$  is the unit vector in edge direction, orthogonal to  $\mathbf{n}$  and  $\boldsymbol{\nu}$ . In the limit of vanishing length, we can rewrite the left-hand side:

$$\begin{aligned} \lim_{\text{length} \rightarrow 0} \int_{\partial A} \mathbf{H}^d \cdot d\mathbf{s} &= \lim_{\text{length} \rightarrow 0} \left\{ \int_{\text{left,right}} (\mathbf{n} \times \mathbf{H}^d) \cdot \boldsymbol{\tau} \, ds + \int_{\text{top,bottom}} (\pm \boldsymbol{\nu} \times \mathbf{H}^d) \cdot \boldsymbol{\tau} \, ds \right\} \\ &= \lim_{\text{length} \rightarrow 0} \int_{\text{left,right}} (\mathbf{n} \times \mathbf{H}^d) \cdot \boldsymbol{\tau} \, ds. \end{aligned} \quad \blacksquare$$



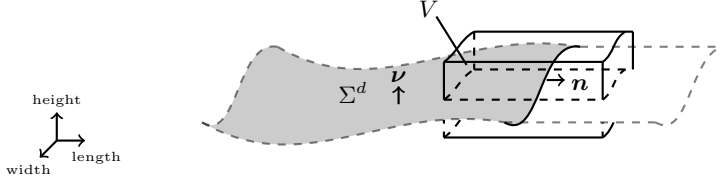


Fig. 6: Choice of rectangular box  $V$ ; a curved, rectangular box containing a part of the edge  $\partial\Sigma^d$ . We extend the sheet over the edge parallel in  $\mathbf{n}$ -direction, and assume  $\sigma^d = 0$  in the extension. The box shall be of vanishing length and height, and with top and bottom faces parallel to the extended sheet  $\Sigma^d$ .

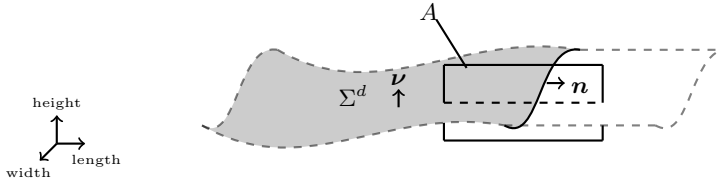


Fig. 7: Choice of area element  $A$ ; a curved, rectangular rectangle enclosing a point of the edge  $\partial\Sigma^d$ . We extend the sheet over the edge parallel in  $\mathbf{n}$ -direction, and assume  $\sigma^d = 0$  in the extension. The area shall be of vanishing length and height, and with top and bottom lines parallel to the extended sheet  $\Sigma^d$ .

Exploiting the fact that  $\mathbf{J} = \mathbf{J}_a + \delta_{\Sigma^d} \sigma^d \mathbf{E}^d + \delta_{\partial\Sigma^d} \lambda^d \mathbf{E}^d$  and by taking the limit of vanishing length we conclude that:

$$(B.2) \quad \lambda^d \mathbf{E}^d \Big|_{\partial\Sigma^d \cap A} \cdot \boldsymbol{\tau} = \lim_{\text{length} \rightarrow 0} \int_{\text{left, right}} (\mathbf{n} \times \mathbf{H}^d) \cdot \boldsymbol{\tau} ds.$$

This implies that the jump over  $\mathbf{n} \times \mathbf{H}^d$  must have a singular point contribution:

$$\left\{ \mathbf{n} \times \mathbf{H}^d \right\}_{\partial\Sigma^d} \cdot \boldsymbol{\tau} = \lambda^d \mathbf{E}^d \Big|_{\partial\Sigma^d \cap A} \cdot \boldsymbol{\tau}.$$

Here, we defined  $\{.\}_{\partial\Sigma^d}$  rigorously as the corresponding limit in (B.2). Note that the height of the area element  $A$  was arbitrarily chosen. Indeed, the actual value of  $\left\{ \mathbf{n} \times \mathbf{H}^d \right\}_{\partial\Sigma^d}$  does not depend on the particular choice of the area element  $A$  because it corresponds directly to a residue of an analytic function  $(\mathbf{n} \times \mathbf{H}^d) \cdot \boldsymbol{\tau}$ . In this sense, Definition (2.3) is an equivalent, slightly less technical definition.

### Appendix C. Derivation of interface and internal boundary condition from weak formulation.

In this appendix we derive the strong formulation with all jump and compatibility conditions starting from a variational formulation. The weak formulation reads, find a

vector field  $E$  such that

$$(C.1) \quad \int_{\Omega} \mu_0^{-1} \nabla \times \mathbf{E}^d \cdot \nabla \times \bar{\psi} \, dx - \omega^2 \int_{\Omega} \varepsilon \mathbf{E}^d \cdot \bar{\psi} \, dx \\ - i\omega \int_{\Sigma^d} \sigma^d \mathbf{E}^d \cdot \bar{\psi} \, dx - i\omega \int_{\partial \Sigma^d} \lambda^d \mathbf{E}^d \cdot \bar{\psi} \, ds = \int_{\Omega} i\omega \mathbf{J}_a \cdot \bar{\psi} \, dx,$$

for all smooth, vector-valued test functions  $\psi$  with compact support in  $\Omega$ . Let us now define

$$(C.2) \quad i\omega \mu_0 \int_{\Omega} \mathbf{H}^d \cdot \bar{\psi} \, dx := \int_{\Omega} \mathbf{E}^d \cdot (\nabla \times \bar{\psi}) \, dx.$$

Integrating (C.2) by parts yields

$$i\omega \mu_0 \int_{\Omega} \mathbf{H}^d \cdot \bar{\psi} \, dx = \int_{\Omega} (\nabla \times \mathbf{E}^d) \cdot \bar{\psi} \, dx - \int_{\Sigma^d} [\boldsymbol{\nu} \times \mathbf{E}^d]_{\Sigma^d} \cdot \bar{\psi} \, d\sigma_x.$$

Thus, testing with (a) a smooth, vector-valued test function  $\psi$  with  $\psi = 0$  on  $\Sigma^d$ , and (b) a sequence  $\psi_h$  of test functions with vanishing support outside  $\Sigma^d$  gives

$$i\omega \mu_0 \mathbf{H}^d = \nabla \times \mathbf{E}^d \quad \text{in } \Omega \setminus \Sigma^d, \quad [\boldsymbol{\nu} \times \mathbf{E}^d]_{\Sigma^d} = 0 \quad \text{on } \Sigma^d.$$

Similarly, integration by parts of (C.1) and substituting  $\mathbf{H}$ :

$$i\omega \int_{\Omega} (\nabla \times \mathbf{H}^d) \cdot \bar{\psi} \, dx - \omega^2 \int_{\Omega} \varepsilon \mathbf{E}^d \cdot \bar{\psi} \, dx - i\omega \int_{\Omega} \mathbf{J}_a \cdot \bar{\psi} \, dx \\ = +i\omega \int_{\Sigma^d} [\boldsymbol{\nu} \times \mathbf{H}^d]_{\Sigma^d} \cdot \bar{\psi} \, d\sigma_x + i\omega \int_{\partial \Sigma^d} \left\{ \mathbf{n} \times \mathbf{H}^d \right\}_{\partial \Sigma^d} \cdot \bar{\psi} \, ds \\ - i\omega \int_{\Sigma^d} \sigma^d \mathbf{E}^d \cdot \bar{\psi} \, d\sigma_x - i\omega \int_{\partial \Sigma^d} \lambda^d \mathbf{E}^d \cdot \bar{\psi} \, ds.$$

The occurrence of the jump term over  $\partial \Sigma^d$  after the integration by parts has to be justified more precisely. Similarly, to the discussion in Appendix B we assume that the function space for  $\mathbf{H}$  admits singular distributions on the edge. More precisely, we define

$$(C.3) \quad \int_{\partial \Sigma^d} \left\{ \mathbf{n} \times \mathbf{H} \right\}_{\partial \Sigma^d} \cdot \psi \, ds := \\ \int_{\Omega} (\nabla \times \mathbf{H}) \cdot \psi \, dx - \int_{\Omega} \mathbf{H} \cdot (\nabla \times \psi) \, dx - \int_{\Sigma^d} [\boldsymbol{\nu} \times \mathbf{H}]_{\Sigma^d} \cdot \psi \, d\sigma_x.$$

Utilizing the same sequences (a) and (b) of test functions yields a similar result:

$$\begin{aligned} \nabla \times (i\omega \mathbf{H}^d) - \omega^2 \varepsilon \mathbf{E}^d - i\omega \mathbf{J}_a &= 0 && \text{in } \Omega \setminus \Sigma^d, \\ i\omega [\boldsymbol{\nu} \times \mathbf{H}^d]_{\Sigma^d} &= i\omega \sigma^d \mathbf{E}^d && \text{on } \Sigma^d \setminus \partial \Sigma^d, \\ i\omega \left\{ \mathbf{n} \times \mathbf{H}^d \right\}_{\partial \Sigma^d} &= i\omega \lambda^d \mathbf{E}^d && \text{on } \partial \Sigma^d. \end{aligned}$$

Now, let  $\varphi$  be an arbitrary scalar-valued test function with compact support and set  $\psi = \nabla \varphi$ . And choose again (a)  $\varphi = 0$  on  $\Sigma^d$ , and (b) a sequence  $\varphi_h$  of test

functions with vanishing support outside  $\Sigma^d$ . Testing (C.2) and subsequent integration by parts results in

$$\nabla \cdot \mathbf{H}^d = 0 \quad \text{in } \Omega \setminus \Sigma^d, \quad \left[ \boldsymbol{\nu} \cdot \mathbf{H}^d \right]_{\Sigma^d} = 0 \quad \text{on } \Sigma^d.$$

In case of the first equation we start again at (C.1). Utilizing the vector identity  $\nabla \times (\nabla \varphi) = 0$ :

$$-\omega^2 \int_{\Omega} \varepsilon \mathbf{E}^d \cdot \nabla \bar{\varphi} \, dx - i\omega \int_{\Sigma^d} \sigma^d \mathbf{E}^d \cdot \nabla \bar{\varphi} \, do_x - i\omega \int_{\partial \Sigma^d} \lambda^d \mathbf{E}^d \cdot \nabla \bar{\varphi} \, ds = i\omega \int_{\Omega} \mathbf{J}_a \cdot \nabla \bar{\varphi} \, dx. \blacksquare$$

Integration by parts:

$$\begin{aligned} \omega^2 \int_{\Omega} \nabla \cdot (\varepsilon \mathbf{E}^d) \bar{\varphi} \, dx + i\omega \int_{\Omega} \nabla \cdot \mathbf{J}_a \bar{\varphi} \, dx \\ = -\omega^2 \int_{\Sigma^d} \left[ \boldsymbol{\nu} \cdot (\varepsilon \mathbf{E}^d) \right]_{\Sigma^d} \bar{\varphi} \, do_x - i\omega \int_{\Sigma^d} \nabla \cdot (\sigma^d \mathbf{E}^d) \bar{\varphi} \, do_x \\ + i\omega \int_{\partial \Sigma^d} \mathbf{n} \cdot (\sigma^d \mathbf{E}^d) \bar{\varphi} \, ds - i\omega \int_{\partial \Sigma^d} \nabla \cdot (\lambda^d \mathbf{E}^d) \bar{\varphi} \, ds. \end{aligned}$$

Here,  $\mathbf{n}$  denotes the outward-pointing unit vector tangential to  $\Sigma^d$  and normal to  $\partial \Sigma^d$ . We point out that for the integration by parts of the interface term  $\int_{\Sigma^d} \sigma^d \mathbf{E}^d$  it is essential that  $\sigma^d$  projects onto the tangential space of  $\Sigma^d$ . We thus recover

$$\nabla \cdot (\varepsilon \mathbf{E}^d) = \frac{1}{i\omega} \nabla \cdot \mathbf{J}_a \quad \text{in } \Omega \setminus \Sigma^d, \quad \left[ \boldsymbol{\nu} \cdot (\varepsilon \mathbf{E}^d) \right]_{\Sigma^d} = \frac{1}{i\omega} \nabla \cdot (\sigma^d \mathbf{E}^d) \quad \text{on } \Sigma^d,$$

and

$$\mathbf{n} \cdot (\sigma^d \mathbf{E}^d) = \nabla \cdot (\lambda^d \mathbf{E}^d) \quad \text{on } \partial \Sigma^d.$$

**Acknowledgments.** We acknowledge support by ARO MURI Award W911NF-14-0247 (MMai, MMat, EK, ML, DM); EFRI 2-DARE NSF Grant 1542807 (MMat); and NSF DMS-1412769 (DM).

REFERENCES

[1] A. ALÙ AND N. ENGHETA, *Achieving transparency with plasmonic and metamaterial coatings*, Phys. Rev. E, 72 (2005), p. 016623, <https://doi.org/10.1103/PhysRevE.72.016623>.  
 [2] Y. AMIRAT AND V. V. SHELUKHIN, *Homogenization of the time harmonic Maxwell equations and the frequency dispersion effect*, Journal de Mathématiques Pures et Appliquées, 95 (2011), pp. 420–443.  
 [3] Y. AMIRAT AND V. V. SHELUKHIN, *Homogenization of time harmonic Maxwell equations: the effect of interfacial currents*, Mathematical Methods in the Applied Sciences, 40 (2017), pp. 3140–3162.  
 [4] D. ARNDT, W. BANGERTH, D. DAVYDOV, T. HEISTER, L. HELTAI, M. KRONBICHLER, M. MAIER, B. TURCK SIN, AND D. WELLS, *The deal.II Library, Version 8.5*, Journal of Numerical Mathematics, 25 (2017), pp. 137–145, <https://doi.org/10.1515/jnma-2017-0058>.  
 [5] A. BENSOUSSAN, J.-L. LIONS, AND G. PAPANICOLAOU, *Asymptotic analysis for periodic structures*, vol. 5 of Studies in Mathematics and its Applications, North-Holland, 1<sup>st</sup> ed., 1978.  
 [6] Y. V. BLUDOV, A. FERREIRA, N. M. R. PERES, AND M. I. VASILEVSKIY, *A primer on surface plasmon-polaritons in graphene*, International Journal on Modern Physics B, 27 (2013), p. 1341001, <https://doi.org/10.1142/S0217979213410014>.

- [7] G. BOUCHITTÉ AND B. SCHWEIZER, *Homogenization of maxwell's equations in a split ring geometry*, Multiscale Modeling & Simulation, 8 (2010), pp. 717–750.
- [8] C. CALOZ, A. LAI, AND T. ITOH, *The challenge of homogenization in metamaterials*, New Journal of Physics, 7 (2005), pp. 167/1–15.
- [9] J. CHENG, W. L. WANG, H. MOSALLAEI, AND E. KAXIRAS, *Surface plasmon engineering in graphene functionalized with organic molecules: A multiscale theoretical investigation*, Nano Letters, 14 (2014), pp. 50–56, <https://doi.org/10.1021/nl403005s>.
- [10] L. A. FALCOVSKY AND S. S. PERSHOGUBA, *Optical far-infrared properties of a graphene monolayer and multilayer*, Physical Review B, 76 (2007), p. 153410.
- [11] Z. FEI, M. D. GOLDFLANN, J.-S. WU, M. WAGNER, A. S. MCLOED, M. K. LIU, K. W. POST, S. ZHU, G. C. A. M. JANSSEN, M. M. FOGLER, AND D. N. BASOV, *Edge and surface plasmons in graphene nanoribbons*, Nano Letters, 15, pp. 8271–8276, <https://doi.org/10.1021/acs.nanolett.5b03834>.
- [12] S. GUENNEAU, F. ZOLLA, AND A. NICOLET, *Homogenization of 3d finite photonic crystals with heterogeneous permittivity and permeability*, Waves in Random and Complex Media, 17 (2007), pp. 653–697.
- [13] X. HUANG, Y. LAI, Z. H. HANG, H. ZHENG, AND C. T. CHAN, *Dirac cones induced by accidental degeneracy in photonic crystals and zero-refractive-index materials*, Nat. Mater., 10 (2011), pp. 582–586.
- [14] S. JAHANI AND Z. JACOB, *All-dielectric metamaterials*, Nature Nanotechnology, 11 (2016), pp. 23–36.
- [15] J. R. KRENN AND J.-C. WEEBER, *Surface plasmon polaritons in metal stripes and wires*, Philosophical Transactions of the Royal Society A, 362 (2004), pp. 739–756, <https://doi.org/10.1098/rsta.2003.1344>.
- [16] G. KRISTENSSON, *Homogenization of corrugated interfaces in electromagnetics*, Progress in Electromagnetics Research, 55 (2005), pp. 1–31.
- [17] P. LALANNE, *Effective medium theory applied to photonic crystals composed of cubic or square cylinders*, Applied Optics, 35 (1996), pp. 5369–5380.
- [18] I. LIBERAL AND N. ENGHETA, *Near-zero refractive index photonics*, Nat. Photon, 11 (2017), pp. 149–158.
- [19] T. LOW, A. CHAVES, J. D. CALDWELL, A. KUMAR, N. X. FANG, P. AVOURIS, T. F. HEINZ, F. GUINEA, L. MARTIN-MORENO, AND F. KOPPENS, *Polaritons in layered two-dimensional materials*, Nature Materials, 16 (2017), pp. 182–194, <https://doi.org/10.1038/nmat4792>.
- [20] M. MAIER, D. MARGETIS, AND M. LUSKIN, *Dipole excitation of surface plasmon on a conducting sheet: finite element approximation and validation*, J. Comput. Phys., 339 (2017), pp. 126–145.
- [21] M. MAIER, D. MARGETIS, AND M. LUSKIN, *Generation of surface plasmon-polaritons by edge effects*, Communications in Mathematical Sciences, 16 (2018), pp. 77–95, <https://doi.org/10.4310/CMS.2018.v16.n1.a4>.
- [22] M. MAIER, D. MARGETIS, AND A. MELLET, *Homogenization of Maxwell's equations in nonhomogeneous plasmonic structures*, Submitted, (2018). Preprint at arXiv:1805.07671 [math.AP].
- [23] M. MAIER, M. MATTHEAKIS, E. KAXIRAS, M. LUSKIN, AND D. MARGETIS, *Universal behavior of dispersive Dirac cone in gradient-index plasmonic metamaterials*, Physical Review B, 97 (2018), <https://doi.org/10.1103/PhysRevB.97.035307>.
- [24] S. A. MAIER, *Plasmonics: Fundamentals and applications*, Springer, New York, 2007.
- [25] M. MATTHEAKIS, C. A. VALAGIANNPOULOS, AND E. KAXIRAS, *Epsilon-near-zero behavior from plasmonic dirac point: Theory and realization using two-dimensional materials*, Physical Review B, 94 (2016), p. 201404(R).
- [26] O. D. MILLER, *Photonic Design: From Fundamental Solar Cell Physics to Computational Inverse Design*, Ph.D. diss., University of California Berkeley, USA, 2012.
- [27] P. MOITRA, Y. YANG, Z. ANDERSON, I. I. KRAVCHENKO, D. P. BRIGGS, AND J. VALENTINE, *Realization of an all-dielectric zero-index optical metamaterial*, Nature Photonics, 7 (2013), pp. 791–795.
- [28] S. MOLESKY, Z. LIN, A. Y. PIGGOTT, W. JIN, J. VUCKOVIĆ, AND A. W. RODRIGUEZ, *Inverse design in nanophotonics*, Nat. Photon, 12 (2018), pp. 659–670.
- [29] C. MÜLLER, *Foundations of the mathematical theory of electromagnetic waves*, Springer-Verlag, New York, 1969.
- [30] A. NEMILENTSAU, T. LOW, AND G. HANSON, *Anisotropic 2d materials for tunable hyperbolic plasmonics*, Phys. Rev. Lett., 116 (2016), p. 066804, <https://doi.org/10.1103/PhysRevLett.116.066804>.

- [31] J. NEVARD AND J. B. KELLER, *Homogenization of rough boundaries and interfaces*, SIAM Journal of Applied Mathematics, 57 (1997), pp. 1660–1686.
- [32] X. NIU, X. HU, S. CHU, AND Q. GONG, *Epsilon-near-zero photonics: A new platform for integrated devices*, Adv. Optical Mater., 6 (2018), p. 1701292.
- [33] G. T. PAPADAKIS, D. FLEISCHMAN, A. DAVOYAN, P. YEH, AND H. A. ATWATER, *Optical magnetism in planar metamaterial heterostructures*, Nature Communications, 9 (2018), p. 296, <https://doi.org/10.1038/s41467-017-02589-8>.
- [34] G. PAVLIOTIS AND A. STUART, *Multiscale methods: Averaging and homogenization*, Springer, 2007.
- [35] V. V. SHELUKHIN AND S. A. TERENCEV, *Frequency dispersion of dielectric permittivity and electric conductivity of rocks via two-scale homogenization of the Maxwell equations*, Progress in Electromagnetics Research B, 14 (2009), pp. 175–202.
- [36] S. N. SHIRODKAR, M. MATTHEAKIS, P. CAZEAUX, P. NARANG, M. SOLJAĆ, AND E. KAXIRAS, *Quantum plasmons with optical-range frequencies in doped few-layer graphene*, Phys. Rev. B, 97 (2018), p. 195435, <https://doi.org/10.1103/PhysRevB.97.195435>.
- [37] M. SILVEIRINHA AND N. ENGHETA, *Tunneling of electromagnetic energy through subwavelength channels and bends using epsilon-near-zero materials*, Phys. Rev. Lett., 97 (2006), p. 157403.
- [38] D. SJÖBERG, C. ENGSTRÖM, G. KRISTENSSON, D. J. N. WALL, AND N. WELLANDER, *A Floquet-Bloch decomposition of Maxwell's equations applied to homogenization*, SIAM Multiscale Modeling and Simulation, 4 (2005), pp. 149–171.
- [39] N. WELLANDER AND G. KRISTENSSON, *Homogenization of the Maxwell equations at fixed frequency*, SIAM Journal on Applied Mathematics, 64 (2003), pp. 170–195.
- [40] D. WINTZ, P. GENEVET, A. AMBROSIO, A. WOOLF, AND F. CAPASSO, *Holographic metalens for switchable focusing of surface plasmons*, Nano Letters, 15 (2015), pp. 3585–3589, <https://doi.org/10.1021/acs.nanolett.5b01076>.
- [41] F. XIA, H. WANG, D. XIAO, M. DUBEY, AND A. RAMASUBRAMANIAM, *Two-dimensional material nanophotonics*, Nat. Photon, 8 (2014), pp. 899–907, <https://doi.org/10.1038/nphoton.2014.271>.
- [42] N. I. ZHELUDEV AND E. PLUM, *Reconfigurable nanomechanical photonic metamaterials*, Nature Nanotechnology, 11 (2016), pp. 16–22.